

REPORT DOCUMENTATION PAGE

AFRL-SR-AR-TR-06-0057

Public reporting burden for this collection of information is estimated to average 1 hour per response, including the time for reviewing instructions, data needed, and completing and reviewing this collection of information. Send comments regarding this burden estimate or any other aspect of this burden to Department of Defense, Washington Headquarters Services, Directorate for Information Operations and Reports (0704-0188), 1215 Jefferson Davis Highway, Suite 1204, Arlington, VA 22202-4302. Respondents should be aware that notwithstanding any other provision of law, no person shall be subject to any penalty for failing to comply with any collection of information if it does not display this OMB control number. **PLEASE DO NOT RETURN YOUR FORM TO THE ABOVE ADDRESS.**

1. REPORT DATE (DD-MM-YYYY) 20-01-2006		2. REPORT TYPE Final		3. DATES COVERED (From - To) Dec 1, 2001 - May 31, 2004	
4. TITLE AND SUBTITLE Hierarchical Modeling of Ferromagnetic SMAs and composites				5a. CONTRACT NUMBER F49620-02-1-0028	
				5b. GRANT NUMBER	
				5c. PROGRAM ELEMENT NUMBER	
6. AUTHOR(S) Minoru Taya, Masahiro Kusaka and Suhasini Gururaja				5d. PROJECT NUMBER	
				5e. TASK NUMBER	
				5f. WORK UNIT NUMBER	
7. PERFORMING ORGANIZATION NAME(S) AND ADDRESS(ES) Department of Mechanical Engineering, CIMS, University of Washington, Box 352600 Seattle, WA 98195-2600				8. PERFORMING ORGANIZATION REPORT NUMBER CIMS-01-2006	
9. SPONSORING / MONITORING AGENCY NAME(S) AND ADDRESS(ES) Air Force Office of Scientific Research 875 N. Randolph Street, Suite 325 Room Arlington, VA 22203 ATTN: Dr Les Lee, Program Manager				10. SPONSOR/MONITOR'S ACRONYM(S) AFOSR	
				11. SPONSOR/MONITOR'S REPORT NUMBER(S)	
12. DISTRIBUTION / AVAILABILITY STATEMENT unlimited				<div style="border: 1px solid black; padding: 10px; display: inline-block;"> <p style="margin: 0;">20060309 061</p> </div>	
<p style="margin: 0;">STATEMENT A Approved for Public Release Distribution Unlimited</p>					
13. SUPPLEMENTARY NOTES					
14. ABSTRACT Ferromagnetic shape memory alloys (FSMA) are key active materials for fast responsive airborne actuators, but the processing cost is rather expensive. IF the hybrid actuation mechanism proposed by Taya is used, we can design cost-effective FSMA composite. This report discusses the design guide for FSMA composites, focusing on several types of actuator, (1) laminated composite plate for bending actuators, and (2) helical spring with optimized cross section for axial actuators. The design guide is given in terms of analytical solutions with closed form. Processing of some of the proposed FSMA composites are also made, and its preliminary data are given.					
15. SUBJECT TERMS					
16. SECURITY CLASSIFICATION OF:			17. LIMITATION OF ABSTRACT	18. NUMBER OF PAGES	19a. NAME OF RESPONSIBLE PERSON
a. REPORT	b. ABSTRACT	c. THIS PAGE			19b. TELEPHONE NUMBER (include area code)

Table of Contents.....	Pages
Chapter 1. Introduction.....	1
Chapter 2. Design of FSMA Composites by Simple Modeling	4
2.1. Modeling on Superelastic behavior of bending composite plates	4
2.2. Analytical Results and Discussion on laminated composite for bending.....	10
2.3. Modeling on superelastic behavior of coil spring made of a composite wire with rectangular cross section	14
2.4. Analytical results and discussion on composite spring.....	21
2.5. Concluding remarks	25
Chapter 3. Modeling of Effective Magnetic and Mechanical Properties of Fe-NiTi Particulate Composite	26
3.1. Composite Magnetic Permeability.....	26
3.2. Saturation Magnetization (M_s^c) of Fe-NiTi particulate composite ..	29
3.3. Stiffness properties of a FSMA composite	31
Chapter 4. Processing of Particulate FSMA Composites	38
Chapter 5. Processing of FSMA Laminated Composites by Plasma Etching/Cladding Method	48
References.....	53
Appendix A: Relation Between Bending Moment and Curvature for Laminated Composites	54
Appendix B: List of Publications and U.S. Patents	61

DISTRIBUTION STATEMENT A
Approved for Public Release
Distribution Unlimited

Chapter 1. Introduction

Ferromagnetic shape memory alloys (FSMAs) have attracted a strong interest among actuator designers as possible fast-responsive compact airborne actuator material. Earlier works on FSMAs were focused on phase transformation of Fe-Pd system [1] and Ni-Mn-Ga system [2] under temperature change. There are three mechanisms of actuation associated with FSMAs, under magnetic field which can be used as driving force for fast responsive actuator materials [3-7]: (i) magnetic field-induced phase transformation, (ii) martensite variant rearrangement and (iii) hybrid mechanism.

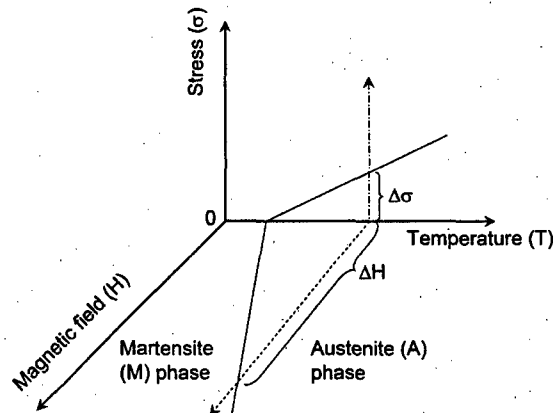


Figure 1. Three dimensional phase transformation diagram of a ferromagnetic shape memory alloy (FSMA) under applied three loading of stress, temperature and magnetic field.

The first mechanism is based on the phase change from austenite to martensite under increasing magnetic field, or reverse phase transformation under decreasing magnetic field. If we can construct three dimensional phase transformation diagram of stress (σ)-temperature (T)-magnetic field (H) axes, see Fig. 1, the phase transformation of austenite to martensite phases under modest magnetic field, requires that the T-H phase boundary surface be inclined toward the T-axis with the T-H boundary line that has a smaller angle with T-axis, otherwise, the increasing H loading would not intersect the T-H phase

boundary surface. Kato et al [8] made preliminary estimate of the necessary magnetic energy to induce a phase transformation based on thermodynamic model, to conclude that large H field is required for the phase change to take for both NiMnGa and FePd. Therefore, this mechanism is not suited for use in designing compact actuators which may need a small and portable electromagnet system as a driving unit.

The second mechanism is to induce the strain in a FSMA with 100 % martensite phase subjected to constant H-field which acts on the magnetic moments in magnetic domains that exist in the martensite phase so as to rotate them along the easy axis, i.e., c-axis in the case of NiMnGa and FePd. The strain induced by this mechanism is a function of c/a ratio of FSMA, i.e., the order of shear strain, given by $a/c - c/a$. Thus, smaller the c/a ratio, the larger shear strain can be induced by this mechanism. The c/a ratio of NiMnGa, is reported to be 0.94, which could provide 6 % or more strain. Recently, Yamamoto et al the reversible straining of a single crystal FePd under a constant magnetic field where the boundary between two kinds of variants are observed to move, contributing to reversible strain of up to 0.49%[9]. Even though the strain induced by the second mechanism is large, the corresponding stress remains to be modest as several MPa under modest applied magnetic flux density (1 T).

The third mechanism which we call as "hybrid mechanism", is based on a set of chain reactions, first applied magnetic flux(or field) gradient, magnetic force, stress induced martensite phase transformation (see Fig 1), resulting in the phase change from stiff austenite to soft martensite phase, leading to large displacement. The advantages of this are large stress (hundred MPa in the case of FePd), modest – intermediate strain, fast actuation time. This phase change can be applied by approaching a compact and portable magnet close to the FSMA specimen which provides a large magnetic field gradient, thus, suited for use in designing actuators with large force capability. Currently, the cost of processing of known FSMA is very high and their mechanical behavior is often unsatisfactory (poor ductility). Also, the processing techniques are quite cumbersome (making single crystals FePd, NiMnGa etc). To overcome these difficulties, we proposed use of FSMA composites with the hybrid actuation mechanism[10] where two cases of

FSAM composite design were discussed, laminated composite for bending type actuators and spring with complicated cross section made of ferromagnetic material and super elastic SMA.

The advantages of the proposed FSMA composites are, fast response, large force and stroke, yet its actuators can be made into compact and light weight with modest material and process costs. As a demonstration, we designed a membrane FSMA composite actuator for use as a new synthetic jet actuator which provided fast jet stream with speed of 190m/sec [11].

This final report states the modeling of FSMA composites in the first two chapters (Chaps. 2 and 3), followed by the processing of laminated and particulate composites in chapter 4 and 5, respectively. Finally, concluding remarks which include future work to be recommended in Chapter 6. Extensive list of references are given at the end, followed by the details of the analytical modeling in Appendix A, and list of publications under this project are given in Appendix B.

Chapter 2. Design of FSMA Composites by Simple Modeling

In this modeling study, two cases of loading, bending and the twist modes of the composites are considered with emphasis on how the geometry and the mechanical properties of the components influence the superelastic(SE) shape memory alloy(SMA) behavior of the composite. First, the bending deformation of the composite plate with application to torque actuators is theoretically analyzed. That is, the relation between the curvature and the bending moment for the composite plate. Next, the spring of the composite wire with the rectangular section form is designed in consideration of application to spring actuators, and the deformation characteristic of the spring is examined. For both models of bending and torsion of FSMA composites, the optimized microstructures of the composites are identified.

2.1. Modeling on Superelastic behavior of bending composite plates

For bending type actuation, the laminated composite plate composed of a ferromagnetic material layer and superelastic SMA layer as shown in Figure 2(a), is examined. The composite plate is subject to bending moment M induced by the magnetic force generated by the ferromagnetic material. After the maximum bending stresses on the plate surface of SMA layer reach the transformation stress (onset of superelastic plateau in the upper loop of the stress-strain curve, Figure 3(b)), the phase transformation proceeds from the plate surface as shown in Figure 2(b). The stress in the transformed region remains constant due to the superelastic behavior of SMA. It is assumed throughout in this paper to facilitate the analysis that the superelastic loop of SMA is "flat" i.e. no working-hardening type slope allowed, and the Young's modulus of the austenite is the same as that of the martensite. These assumptions would allow us to obtain closed form solutions in the present model, although the predictions are still to the first order approximation. The aim of using this simple model is to identify the best thickness ratio of a ferromagnetic layer and SMA layer in the composite plate.

Then, the relation between the bending moment and the curvature is theoretically calculated by using stress-strain curves of the constituent materials. Figure 3(a) shows the analytical model. Radius of curvature of the composite plate subject to bending moment

M is ρ , the thickness of the composite plate is h , the thickness of the ferromagnetic layer is h_f , and the plate width is b . Figure 3(b) shows the stress-strain curves of the ferromagnetic material and the superelastic SMA, where the Young's modulus of the ferromagnetic material is E_f , that of the SMA are E_{SMA} , the yield stress of the ferromagnetic material is σ_f , and only elastic portion of the ferromagnetic material is shown. The onset stress for phase transformation of superelastic SMA is σ_0 , the onset stress for reverse transformation is σ_1 in the superelastic loop portion of SMA. As a result, the relation between the bending moment and the curvature of the composite plate also is expected to exhibit the superelastic loop if properly designed. This superelastic loop of the ferromagnetic shape memory alloy composites is indeed desired.

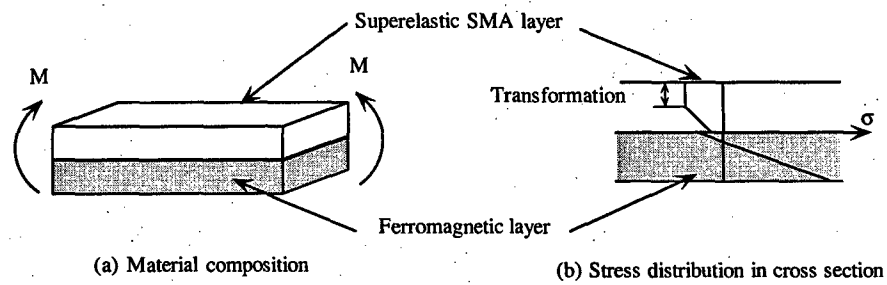


Figure 2. Composite plate for bending mode actuation.

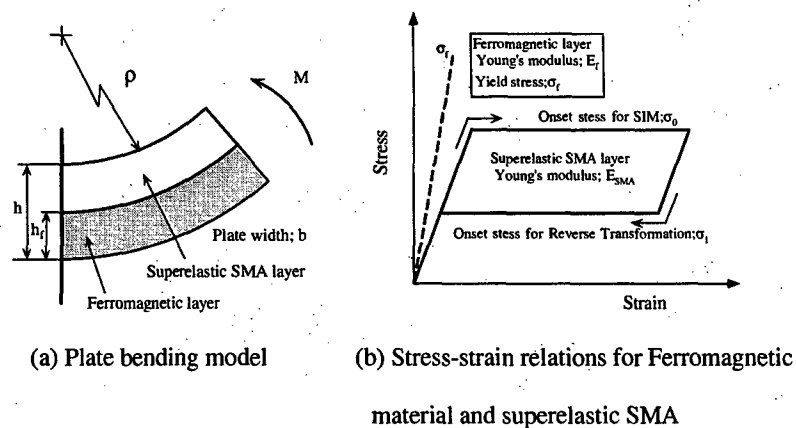


Figure 3. Material properties and model for the theoretical examination.

The curvature which reaches yield stress σ_f in a ferromagnetic layer and the curvature which reaches transformation stress σ_0 in superelastic SMA layer are strongly influenced by the mechanical properties and the thickness of both materials. Stress distribution is classified into the following three cases because of the relation between the transformation stress in the SMA layer and the yield stress of a ferromagnetic layer.

Case 1: The stress in a ferromagnetic layer reaches the yield stress σ_f , before reaching the transformation stress σ_0 in the superelastic SMA layer.

The stress distribution of this case upon loading and unloading is shown in Figure 4, where the bending stress by elastic deformation is illustrated in each material.

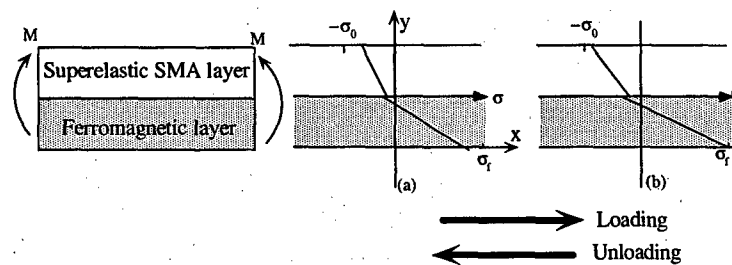


Figure 4. Changes in stress distribution in cross section according to load (Case 1)

Case 2: The stress in a ferromagnetic layer reaches the yield stress, after SMA layer reaching the transformation stress in some part.

The stress distribution of Case 2 upon loading and unloading is shown in Figure 5. Under increasing bending moment first elastic stress distribution (a), then the stress in the SMA layer reaches the transformation stress σ_0 at the position of y_1 (b), and when the transformation domain advances to $y_1=Y_1$, a ferromagnetic layer reaches the yield stress σ_f (c). It is noted in (b)-(e) that Y_1 remains constant until y_3 reaches Y_1 . During unloading, the stress decreases first in elastically in all domains (d); next, the stress becomes constant from the upper part of the SMA layer to the position of y_3 where the

stress reached reverse transformation stress σ_1 (e). In addition, after the stress at location $y_3=Y_1$ reaches σ_1 , the stress inside portion ($y < y_2$) decreases elastically (f). Finally, the stress in the entire SMA layer decreases elastically when the stress in the SMA on the top surface becomes small than σ_1 (g).

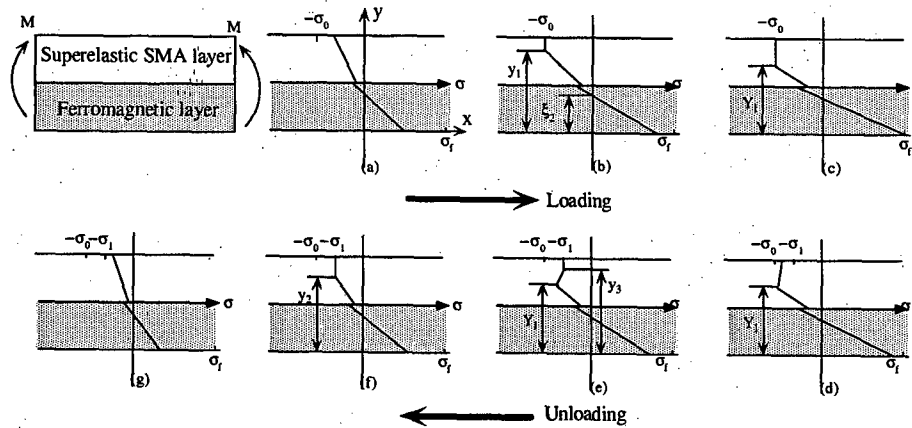


Figure 5. Changes in stress distribution in cross section according to load (Case 2)

Case 3: The stress in a ferromagnetic layer reaches the yield stress, after the entire domain of the superelastic SMA layer reaching the transformation stress σ_0 .

The stress distribution of Case 3 upon the loading and the unloading is shown in Figure 6. In early stage of loading, the stress in a ferromagnetic layer does not reach the yield stress yet even after the stress in all domains of the SMA layer reaches the transformation stress σ_0 (c). A neutral axis position changes with an increase in the load, and the stress reaches the yield stress σ_f finally in a ferromagnetic layer (d). The process of unloading is shown in Figure 6 (e) to (h).

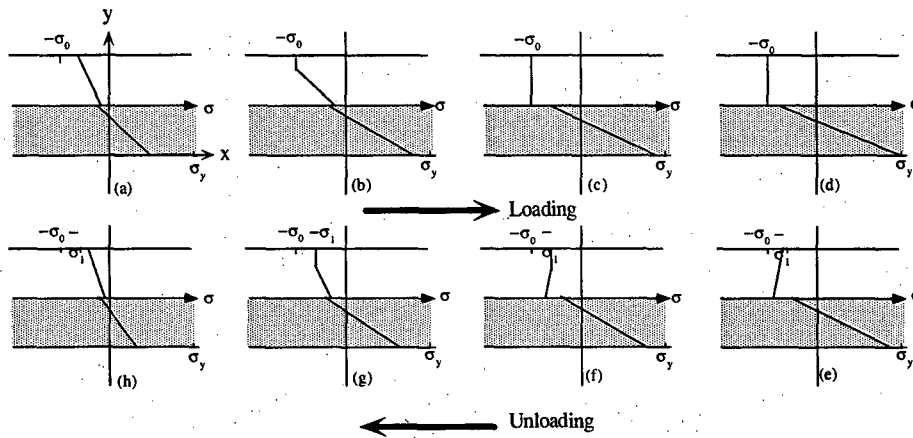


Figure 6. Changes in stress distribution in cross section according to load (Case 3)

For each stress distribution $\sigma_x(y)$ of the three cases, the following equations are valid, i.e. the equilibrium of force and moment.

$$\int_0^h \sigma_x(y) y dy = 0 \quad (1)$$

$$M = - \int_0^h \sigma_x(y) y b dy \quad (2)$$

The neutral axis position and the relation between the moment and the curvature are obtained by solving these equations. Let us focus on the case 2, particularly the stress state of figure 5(b). When a neutral axis position is ξ_2 , and the transformation stress position is y_1 , the stress distribution in each domain becomes in ferromagnetic layer ($0 < y < h_f$)

$$\sigma(y) = E_f \frac{\xi_2 - y}{\rho} \quad (3)$$

in SMA layer below the transformation stress σ_0 ($h_f < y < y_1$)

$$\sigma(y) = E_{SMA} \frac{\xi_2 - y}{\rho} \quad (4)$$

in the transformation domain of SAM ($y_1 < y < h$)

$$\sigma(y) = -\sigma_0 \quad (5)$$

By substituting Eqs. (3), (4), and (5) to Eqs. (1) and (2), unknown ξ_2 and y_1 are solved and they are given by

$$\frac{\xi_2}{h} = \left\{ \left(\frac{E_f}{E_{SMA}} - 1 \right) \frac{h_f}{h} + \frac{\sigma_0 \rho}{E_{SMA} h} \right\} + \sqrt{ \frac{E_f}{E_{SMA}} \left(\frac{E_f}{E_{SMA}} - 1 \right) \left(\frac{h_f}{h} \right)^2 + 2 \frac{\sigma_0 \rho}{E_{SMA} h} \left\{ 1 + \left(\frac{E_f}{E_{SMA}} - 1 \right) \frac{h_f}{h} \right\} } \quad (6)$$

$$\frac{y_1}{h} = \frac{\xi_2}{h} + \frac{\sigma_0 \rho}{E_{SMA} h} \quad (7)$$

Moreover, by substituting Eqs. (3)-(7) to Eq. (2), the relation between the normalized bending moment and curvature is obtained as

$$\frac{M}{E_{SMA} b h^2} = \frac{h}{\rho} \left[\frac{E_f}{E_{SMA}} \left\{ \frac{1}{3} \left(\frac{h_f}{h} \right)^3 - \frac{1}{2} \frac{\xi_2}{h} \left(\frac{h_f}{h} \right)^2 \right\} + \frac{1}{3} \left\{ \left(\frac{y_1}{h} \right)^3 - \left(\frac{h_f}{h} \right)^3 \right\} - \frac{1}{2} \frac{\xi_2}{h} \left\{ \left(\frac{y_1}{h} \right)^2 - \left(\frac{h_f}{h} \right)^2 \right\} \right] + \frac{1}{2} \frac{\sigma_0}{E_{SMA}} \left\{ 1 - \left(\frac{y_1}{h} \right)^2 \right\} \quad (8)$$

Eq. (8) is valid for the range of curvature, i.e. from the curvature with transformation stress σ_0 in top ($y=h$) of SMA layer to the curvature with yield stress σ_f at bottom ($y=0$) of ferromagnetic layer. This range of the curvature is given by

$$\frac{\sigma_0}{E_{SMA}} \frac{2 \left\{ 1 + \left(\frac{E_f}{E_{SMA}} - 1 \right) \left(\frac{h_f}{h} \right) \right\}}{1 + \left(\frac{E_f}{E_{SMA}} - 1 \right) \left(2 - \frac{h_f}{h} \right) \left(\frac{h_f}{h} \right)} < \frac{h}{\rho} \leq \frac{h}{\rho_1} \quad (9)$$

where

$$\frac{h}{\rho_1} = \frac{\left(\frac{\sigma_f + \sigma_0}{E_f + E_{SMA}} \right)^2}{- \left\{ \frac{\sigma_f}{E_f} \left(\frac{E_f}{E_{SMA}} - 1 \right) \frac{h_f}{h} - \frac{\sigma_0}{E_{SMA}} \right\} + \sqrt{ \left\{ \frac{\sigma_f}{E_f} \left(\frac{E_f}{E_{SMA}} - 1 \right) \frac{h_f}{h} - \frac{\sigma_0}{E_{SMA}} \right\}^2 + \left(\frac{\sigma_f + \sigma_0}{E_f + E_{SMA}} \right)^2 \left(\frac{E_f}{E_{SMA}} - 1 \right) \left(\frac{h_f}{h} \right)^2 }} \quad (10)$$

Similarly, the relations between the bending moment and the curvature for the three cases of Figs. 4-6 can be calculated. The results for cases 1, 2 and 3 are shown in APPENDIX. The conditions under which three cases are valid, are obtained as

Case 1

$$\frac{\sigma_f}{\sigma_0} < \frac{E_f}{E_{SMA}} \frac{1 + \left(\frac{E_f}{E_{SMA}} - 1 \right) \left(\frac{h_f}{h} \right)^2}{1 + \left(\frac{E_f}{E_{SMA}} - 1 \right) \left(2 - \frac{h_f}{h} \right) \left(\frac{h_f}{h} \right)} \quad (11)$$

Case 2

$$2 \frac{h}{h_f} \left\{ \frac{\sigma_0}{E_{SMA}} + \frac{\sigma_0}{E_f} \left(\frac{h_f}{h} - 1 \right) \right\} > \frac{h}{\rho_1} \quad (12)$$

Case 3

$$2 \frac{h}{h_f} \left\{ \frac{\sigma_0}{E_{SMA}} + \frac{\sigma_0}{E_f} \left(\frac{h_f}{h} - 1 \right) \right\} \leq \frac{h}{\rho_1} \quad (13)$$

The maximum normalized curvatures in these cases are given by

$$\begin{array}{ccc} \text{Case 1} & \text{Case 2} & \text{Case 3} \\ \frac{h}{\rho} = \frac{\sigma_f}{E_f} \frac{2 \left\{ 1 + \left(\frac{E_f}{E_{SMA}} - 1 \right) \left(\frac{h_f}{h} \right) \right\}}{1 + \left(\frac{E_f}{E_{SMA}} - 1 \right) \left(\frac{h_f}{h} \right)^2}, & \frac{h}{\rho} = \frac{h}{\rho_1}, & \frac{h}{\rho} = 2 \frac{h}{h_f} \left\{ \frac{\sigma_f}{E_f} - \frac{\sigma_0}{E_f} \left(\frac{h_f}{h} - 1 \right) \right\} \end{array} \quad (14)$$

The maximum deformability of the composite plate can be analyzed for a given set of the mechanical properties and the thickness ratio of materials by using equation (14).

2.2. Analytical Results and Discussion on laminated composite for bending

The relation between the bending moment and the curvature is predicted by the present model for two type of the composite, i.e. Fe/CuAlMn and FeCoV/CuAlMn. Figure 7(a) is the idealized stress-strain curves of Fe and CuAlMn. The results of the predicted relation between the normalized bending moment and the normalized curvature for thickness ratio $h_f/h=0.5$ are shown in Figure 7(b). The state of the stress for this case corresponds to Case 1, Fig.4, i.e. the stress in SMA layer is not superelastic plateau, thus, the superelastic loop is not observed as evidenced in Figure 7(b). Therefore, the composite plate of Fe and CuAlMn is undesirable as effective bending actuator component.

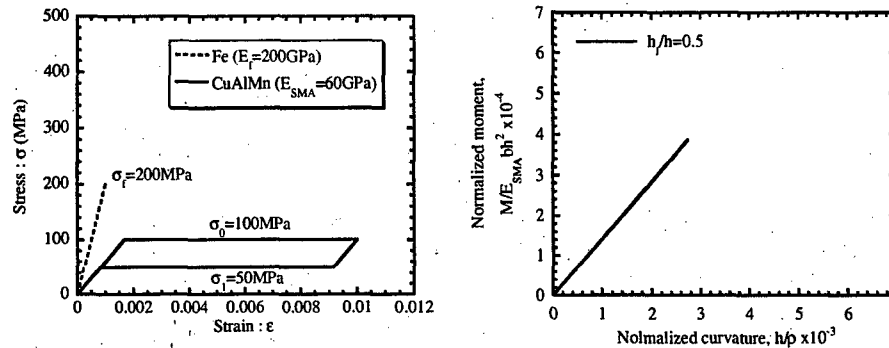


Figure 7. (a) Stress-strain curve for Fe and (b) Relation between normalized bending moment and normalized curvature for CuAlMn-Fe composite.

Next, the FeCoV/CuAlMn composite plate was analyzed by using the mechanical property data shown in Figure 8(a). Figure 8(b) shows the analytical results for $h_f/h=0.5$, exhibiting clearly superelastic behavior. By using FeCoV whose yield stress is larger than Fe, yet its soft magnetic property is better than Fe, we can achieve now the state where most of the CuAlMn layer becomes a transformation domain, corresponding to almost the state of Case 3. Moreover, the maximum curvature was 2.22 times larger and the bending moment was 1.60 times larger than those of the composite with Fe. Therefore, the FSMA composite so identified is promising as an effective bending actuator component.

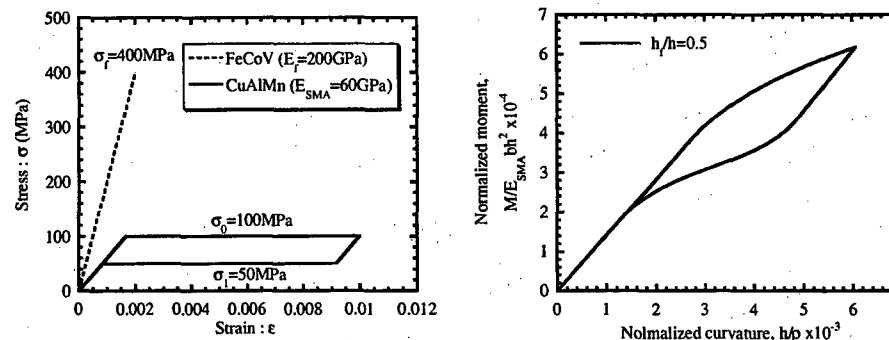
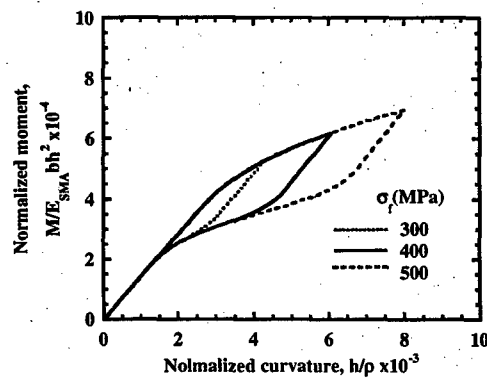
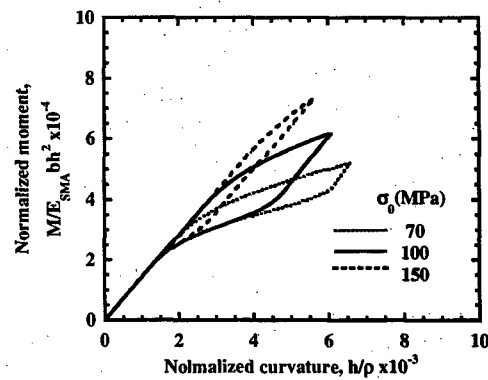


Figure 8. (a) Stress-strain curve for FeCoV, (b) Relation between normalized bending moment and normalized curvature for CuAlMn-FeCoV composite.

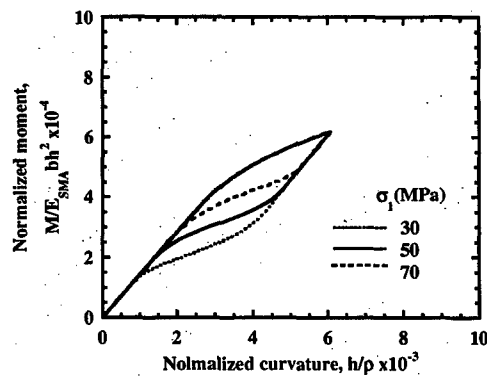
Next, we performed a set of parametric studies to examine the effects of material parameters (σ_f , E_f , σ_0 , σ_1 , E_{SMA}) and geometrical parameter, i.e., thickness ratio (h_f/h). The predicted results are shown in Figure 8, where (a)-(f) denote the case of changing parameters, yield stress of ferromagnetic material (σ_f), the upper plateau stress (σ_0) and lower plateau stress (σ_1) of CuAlMn superelastic loop, and ratio of ferromagnetic plate (h_f) to the composite (h), h_f/h , Young's modulus of ferromagnetic material (E_f) and that of SMA (E_{SMA}), respectively.



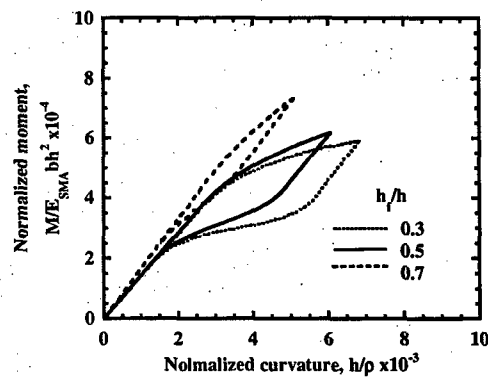
(a) σ_f



(b) σ_0



(c) σ_1



(d) h_f/h

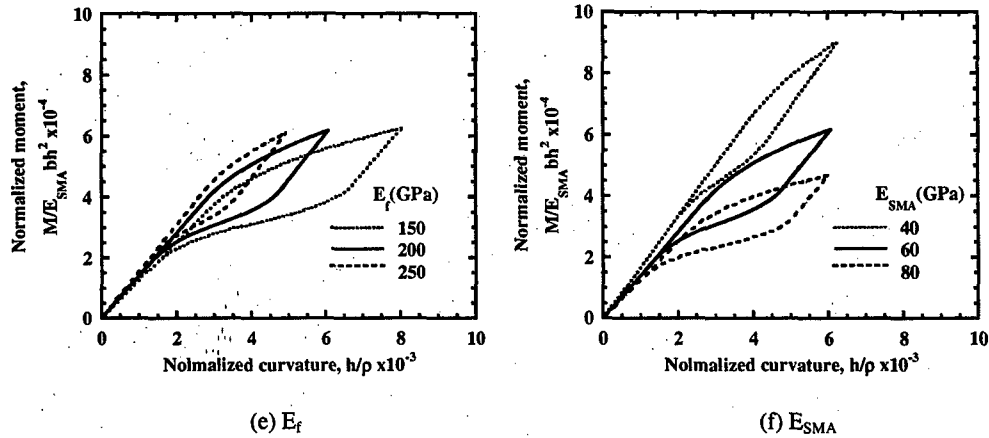
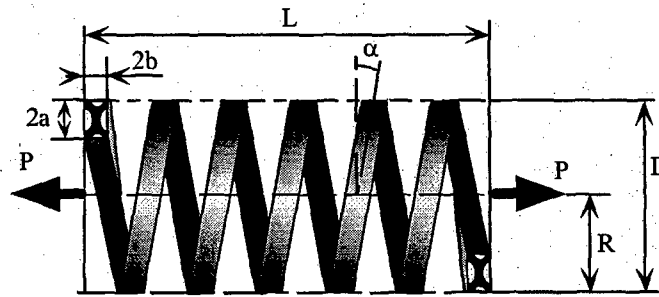


Figure 9. Change in superelastic behavior of bending plate influenced by various parameters, (a) yield stress of Fe, (b) upper transformation stress of SMA, (c) lower transformation stress of SMA, (d) thickness ration of Fe to FSMA composite, (e) Young's modulus of Fe and (f) Young's modulus of SMA.

When the yield stress of the ferromagnetic material increases, it is clear from Figure 9(a) that both bending moment and the curvature increase. When transformation stress σ_0 of SMA increases, it is found from Figure 9(b) that the bending moment increases and the curvature decreases. It can be seen from Figure 9(c), the lower limit of the superelastic loop decreases if the reverse transformation stress σ_1 decreases. When the thickness of the ferromagnetic layer increases, it is clear from Figure 9(d) that the bending moment increases though the curvature decreases. Oppositely, because the thickness of superelastic SMA layer increases when the thickness of a ferromagnetic layer decreases, the superelasticity behavior increases. Therefore, the bending moment decreases, and the curvature increases. From Figure 9(e), the maximum curvature decreases though the bending moment does not change when the Young's modulus of the ferromagnetic material increases. Therefore, an increase in the Young's modulus of the ferromagnetic material is undesirable as the composite. From Figure 9(f), the bending moment decreases when the Young's modulus of SMA increases. The design of a more high performance ferromagnetic shape memory alloy composites becomes possible by the materials design based on the above analysis.

2.3. Modeling on superelastic behavior of coil spring made of a composite wire with rectangular cross section

With the aim of designing a high-speed linear actuator, the superelastic characteristic of a coiled spring of the ferromagnetic shape memory composite wire with rectangular section is analyzed. Figure 9 shows the analytical model. The magnetic force is generated in the ferromagnetic material by the magnetic field gradient, and displacement is generated in the spring by the hybrid mechanism described in Introduction. The relation between this spring force and displacement is analyzed.



D: the diameter of spring ($D=2R$)

d: the diameter of wire

p: the pitch of one cycle

n: the number of turns

L: the length of spring without load ($L=np$)

α : the inclined angle of the wire to the x-y plane

Figure 10. Analytical model of coil spring with rectangular cross section.

When axial force P is given to the spring, the wire of the ferromagnetic shape memory composite is subjected to torque T . The relation between spring force P and torque T is given by the next equation by

$$T = PR \cos \alpha \quad (15)$$

for a twist angle per unit length of the rectangular section wire of ω , the total twist angle ϕ is $2\pi R\omega \sec\alpha$ as the total length of the wire is $2\pi R \sec\alpha$. Therefore, the displacement of the spring is calculated by the next equation.

$$\begin{aligned}\delta &= \delta_{torsion} + \delta_{shear} \cong \delta_{torsion} \\ &= R\phi = 2\pi R^2 \omega \sec\alpha\end{aligned}\quad (16)$$

It is assumed in the present model that the displacement due to direct shear, δ_{shear} is neglected. This is justified for large ratio of D to a or b . Then, the relation between the spring force, P and displacement, δ can be calculated if the relation between the twist angle per unit length ω and the torque T of the rectangular section wire is known, which will be obtained in the following.

Analytical Model for Torsion of Composite Wire with Rectangular Section

To generate large magnetic force by the hybrid mechanism, it is necessary to increase the area of a ferromagnetic material in the rectangular section, while meeting the requirement that the ferromagnetic material should not reach its yield stress. The stress field in the rectangular section can be calculated from the shear strain distribution of the rectangular section for a given twist angle.

Let us look at the rectangular section of a composite with width $2a$ and height $2b$ as showing in Figure 11. We introduce the assumption that the spring deformation is uniform along the wire direction (z -axis) and plane displacements u and v are in proportion to z , as follows;

$$u = -\omega yz, \quad v = \omega xz, \quad w = \omega \varphi(x, y) \quad (17)$$

where the function $\varphi(x, y)$ is the Saint-Venant's function [11] that satisfies the equilibrium equation and 2D compatibility equation of strain. For the spring with rectangular cross section, the shear strain components are expressed as

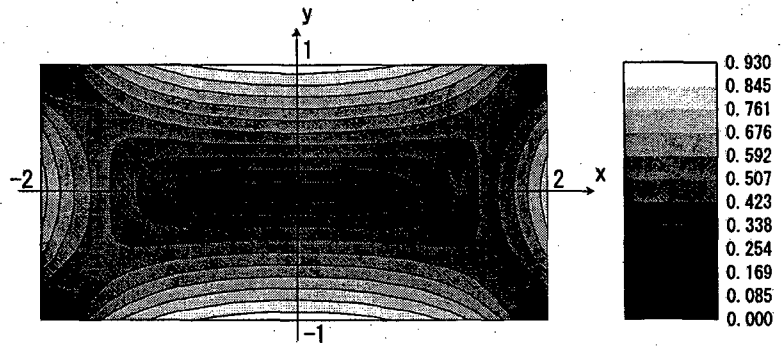
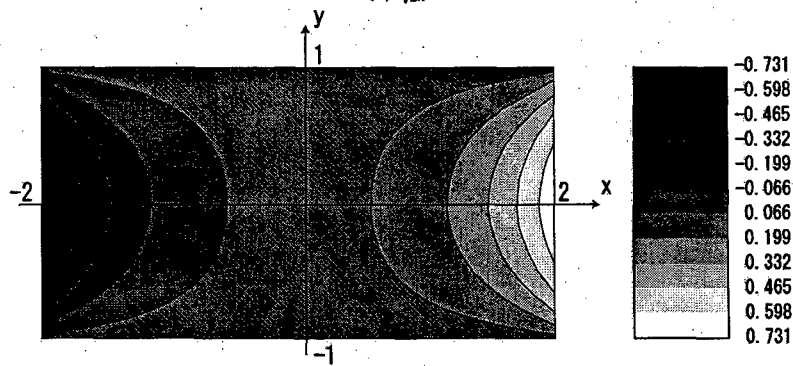
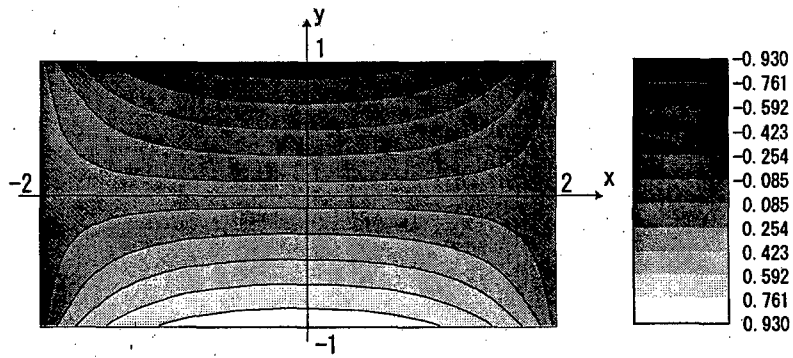


Figure 11. Contour line distributions of shear strain in rectangular section, (a) $\gamma_{zx}/a\omega$, (b) $\gamma_{zy}/a\omega$ and (c) $\gamma/a\omega$, where a is the length of longer side of a rectangular cross section of a FSMA composite and ω is the twist angle per unit length.

$$\frac{\gamma_{zx}}{\omega a} = -\frac{16}{\pi^2} \sum_{n=1}^{\infty} \frac{(-1)^{n-1}}{(2n-1)^2} \frac{\sinh[(2n-1)\pi y/2a]}{\cosh[(2n-1)\pi b/2a]} \cos[(2n-1)\pi x/2a] \quad (18)$$

$$\frac{\gamma_{zy}}{\omega a} = \frac{16}{\pi^2} \sum_{n=1}^{\infty} \frac{(-1)^{n-1}}{(2n-1)^2} \left\{ 1 - \frac{\cosh[(2n-1)\pi y/2a]}{\cosh[(2n-1)\pi b/2a]} \right\} \sin[(2n-1)\pi x/2a] \quad (19)$$

Therefore, the effective shear strain acting on the rectangular cross section, γ is calculated by

$$\gamma = \sqrt{\gamma_{zx}^2 + \gamma_{zy}^2} \quad (20)$$

For $a=2$ and $b=1$, the contour line distributions of shear strain component γ_{zx} , γ_{zy} and effective shear strain γ divided by $a\omega$ are shown in Figure 11(a), (b) and (c) respectively. γ_{zx} becomes 0 at $x=-a$ and a , and it reaches to the minimum value at $y=b$ on the y axis, and becomes the maximum at $y=-b$ on the y axis. γ_{zy} reaches to the minimum value at $x=-2$, $y=0$, and becomes the maximum at $x=2$, $y=0$. The normalized effective shear strain, $\gamma/a\omega$ reaches the maximum value 0.930 at the center of long side edges, and reduces toward the center.

The effective shear stress induced in the ferromagnetic material is calculated by multiplying γ by the shear modulus G_f of the ferromagnetic material. The effective shear stress distribution of the ferromagnetic material in the rectangular section is calculated for a given set of twist angle per unit length ω , size a and b . Then, the optimum shape of the ferromagnetic material can be determined from its domain under the condition that the effective shear stress does not exceed the yield stress in shear τ_f of the ferromagnetic material.

If FeCoV ($G_f=70\text{GPa}$, $\tau_f=231\text{MPa}$) is used as a ferromagnetic material, and CuAlMn is used as a superelastic SMA, then for $\omega=0.003$, $a=2$, and $b=1$, $\gamma/\omega a < 0.55$ is obtained from the requirement of $G_f \gamma < \tau_f$. Figure 11 shows the optimized rectangular section of the composite obtained by this design, where the dark area of FeCoV satisfies $\gamma/\omega a < 0.55$.

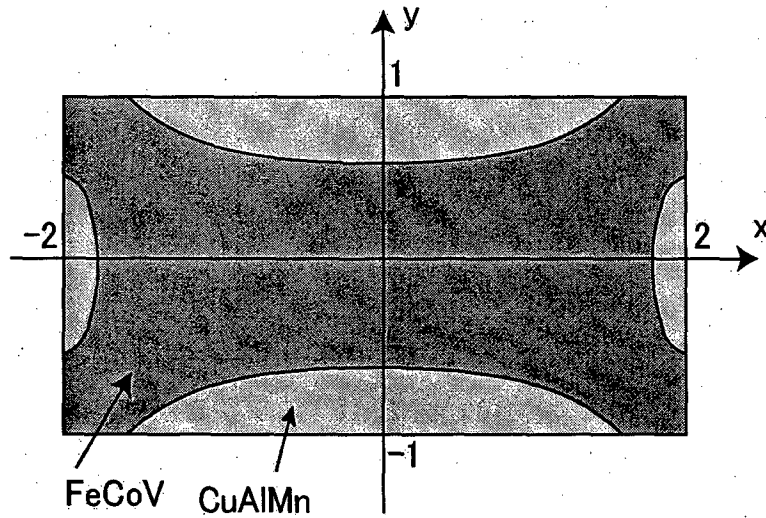


Figure 12. Optimized rectangular section of the composite made of ferromagnetic, FeCoV and superelastic SMA, CuAlMn.

Next, we examine the relation between the twist angle per unit length ω and the torque T of the composite wire with rectangular section. The torque is calculated by

$$\begin{aligned}
 T = M_z = PR \cos \alpha &= \int_{-b}^b \int_{-a}^a (x\tau_{zy} - y\tau_{zx}) dx dy \\
 &= \int_{-b}^b \int_{-a}^a G(x\gamma_{zy} - y\gamma_{zx}) dx dy
 \end{aligned} \tag{21}$$

Here, we can define three domains in the composite during loading.

Domain 1: Domain of ferromagnetic material

Domain 2: Domain with effective shear stress less than the forward transformation shear stress of SMA, τ_0

Domain 3: Transformation domain of SMA

The effective stress in the ferromagnetic material is obtained by multiplying shear modulus G_f by the corresponding effective shear strain for the elastic deformation. In SMA, it is necessary to judge if the effective shear stress τ is below the forward transformation shear stress τ_0 . τ is obtained by multiplying shear modulus G_{SMA} by γ if the effective shear stress of domain 2 is below the forward transformation shear stress τ_0 . In domain 3 where the effective shear stress τ reaches the upper transformation shear stress τ_0 , then $\tau = \tau_0$.

Because a shear strain component proportionally increases with an increase in ω , by multiplying the corresponding shear strain component by the modified shear modulus $G = \tau_0/\gamma$, the shear stress component for which τ becomes τ_0 is calculated. That is, Equation (21) is applicable to domain 3 by using Equation (24). Then, torque T corresponding to the twist angle per unit length ω is calculated by equation (21) by using the modified shear modulus in each domain according to the following Eqs.

$$\text{Domain 1: } \gamma < \frac{\tau_f \omega}{G_f \omega_f}$$

$$G = G_f \tag{22}$$

$$\text{Domain 2: } \gamma \geq \frac{\tau_f \omega}{G_f \omega_f} \text{ and } \gamma < \frac{\tau_0}{G_{SMA}}$$

$$G = G_{SMA} \tag{23}$$

$$\text{Domain 3: } \gamma \geq \frac{\tau_f \omega}{G_f \omega_f} \text{ and } \gamma \geq \frac{\tau_0}{G_{SMA}}$$

$$G = \frac{\tau_0}{\gamma} \tag{24}$$

where, ω_f is input data, and it is the maximum twist angle per unit length when the cross section is optimized, $\omega_f = 0.0015$ for cross section shape of Figure 12.

Next, the case of unloading is considered. The stress in each domain decreases during the unloading, but the superelasticity in SMA was generated in domain 3 where the effective shear stress reached the transformation stress during the preceding loading, it is necessary to divide domain 3 into three sub-domains.

Domain 3-1: τ above the reverse transformation stress τ_1

Domain 3-2: τ equal to the reverse transformation stress τ_1

Domain 3-3: τ below the reverse transformation stress τ_1

For domain 3-1, the effective shear stress τ is larger than the reverse transformation stress τ_1 . The shear stress component of $\tau=\tau_0$ is calculated by multiplying modified shear modulus of Equation (24) by the shear strain component, and it decreases from this stress state elastically in proportion to G_{SMA} in domain 3. That is, the shear stress component is calculated by multiplying the modified shear modulus of Equation (26) by the shear strain component in the range of the effective shear strain of Equation (25).

$$\text{Domain 3-1 } \gamma > \frac{\tau_1}{G_{SMA}} \text{ and } \gamma \leq \frac{(\tau_0 - \tau_1)\omega}{G_{SMA}(\omega_f - \omega)} \quad (25)$$

$$G = \frac{\tau_0}{\gamma} - G_{SMA} \quad (26)$$

For domain 3-2, because the effective shear stress reaches the reverse transformation stress τ_1 , the shear stress remains constant, i.e. $\tau=\tau_1$. That is, the shear stress is calculated by multiplying the modified shear modulus of Equation (28) by the shear strain in the range of effective shear strain of Equation (27).

$$\text{Domain 3-2 } \gamma > \frac{\tau_1}{G_{SMA}} \text{ and } \gamma > \frac{(\tau_0 - \tau_1)\omega}{G_{SMA}(\omega_f - \omega)} \quad (27)$$

$$G = \frac{\tau_1}{\gamma} \quad (28)$$

For domain 3-3, the superelasticity disappears because the effective shear stress lowers more than τ_1 . The range of effective shear strain and modified shear modulus are given by

$$\text{Domain 3-3 } \gamma \leq \frac{\tau_1}{G_{SMA}} \quad (29)$$

$$G = G_{SMA} \quad (30)$$

The torque T corresponding to ω can be analyzed from equation (21) by calculating effective shear strain of each area using the modified shear modulus corresponding to each domain defined by Equations (22), (23), (24), (26), (28) and (30). The relation between the force and displacement of a spring can be calculated by using Equation (15) and (16).

2.4. Analytical results and discussion on composite spring

Based on the above model, we made predictions of the torque (T) - twist angle (ω) relation, and also of the spring force (P) - displacement (δ) relation where the idealized stress-strain relations of ferromagnetic FeCoV and superelastic CuAlMn shown in Figure 13 are used.

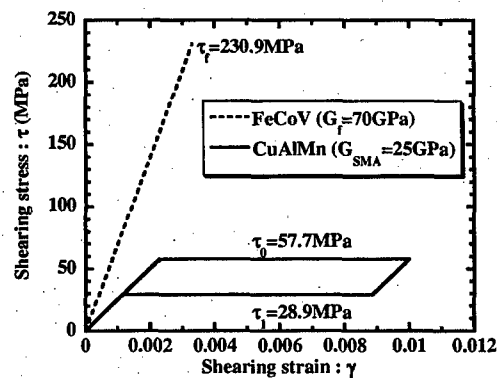


Figure 13. Idealized stress-strain curves of FeCoV and CuAlMn.

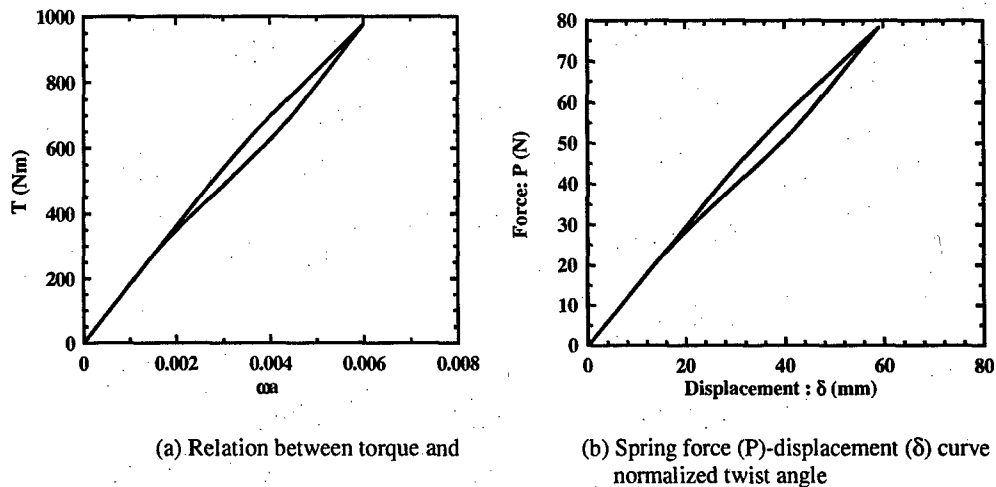


Figure 14. Superelastic behavior of Fe/CuAlMn composite spring.

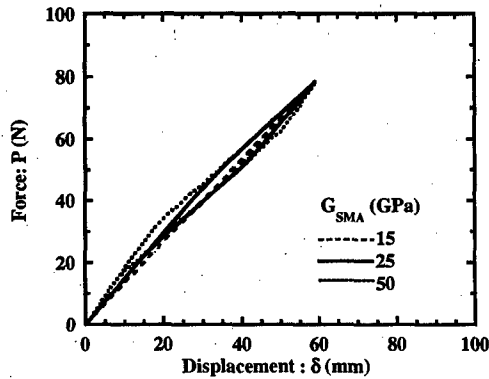
Figure 14 show the analytical results for the case of maximum twist angle per unit length $\omega=0.003$ of a composite plate wire with $a=2\text{mm}$ (width is 4mm), and $b=1\text{mm}$ (height is 2mm). Figure 14(a) shows the relation between the torque and the normalized twist angle, indicating that the torque rises proportionally as the twist angle increases, and the transformation of SMA begins at $\omega a=0.0025$, reaching the transformation stress with $\omega a=0.0042$ in all domain of SMA. After ωa reaches 0.006 , the superelastic loop exhibits the reverse transformation corresponding to the unloading.

Figure 14(b) shows the relation between the spring force and the displacement of the coil spring of length $L=100\text{mm}$, diameter $D=25\text{mm}$, pitch $p=5\text{mm}$ and number of turns $n=20$. The maximum displacement of this coiled spring was 59.2mm , the spring force became 78.4N .

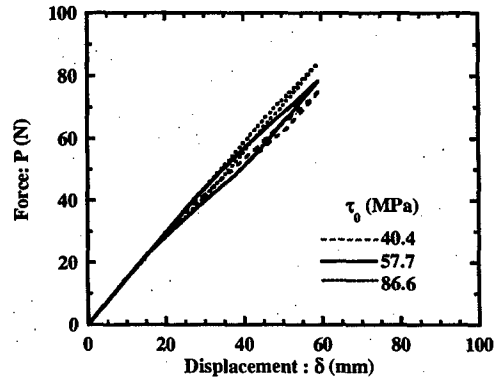
We made a parametric study to examine the effects of each parameter on the P- δ relation. Figure 15 shows the analytical results of the P- δ relations influenced by various parameters, (a) G_{SMA} , (b) τ_0 , (c) G_f , (d) τ_f and (e) τ_1 . From Figure 15 (a), it is clear that shear modulus of superelasticity SMA does not influence the maximum displacement and the maximum spring force. It is noted from Figure 15 (b), that the spring force increases with an increase in forward transformation shear stress τ_0 . It is clear from Figure 15 (c),

that the spring force does not change and only the maximum displacement increases if the shear modulus of the ferromagnetic material becomes small resulting in larger displacement of the spring. It can be seen from Figure 15 (d), that both the spring force and displacement increase the superelastic behavior when the yield stress of the ferromagnetic material increases. It is noted from Figure 15 (e), that the lower limit of superelastic loop decreases if the reverse transformation stress τ_1 decreases.

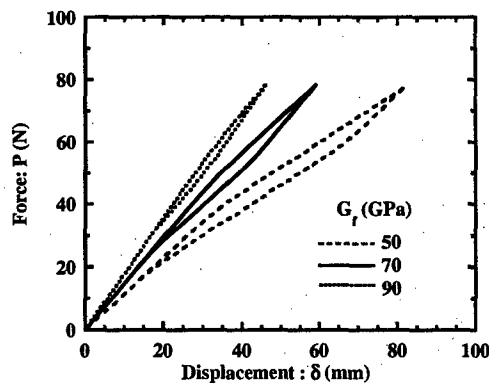
In summary, larger τ_f of the ferromagnetic material and softer ferromagnetic material will provide a spring actuator with larger displacement. And, to obtain large force of the spring, use of SMA of larger τ_0 is desired.



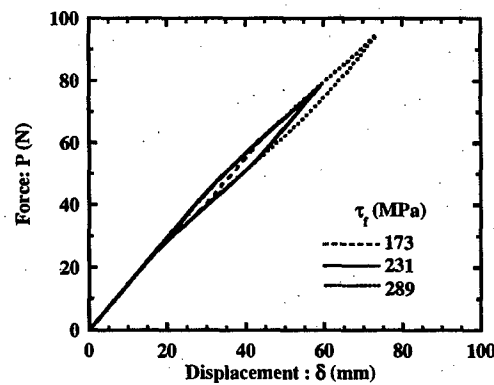
(a) G_{SMA}



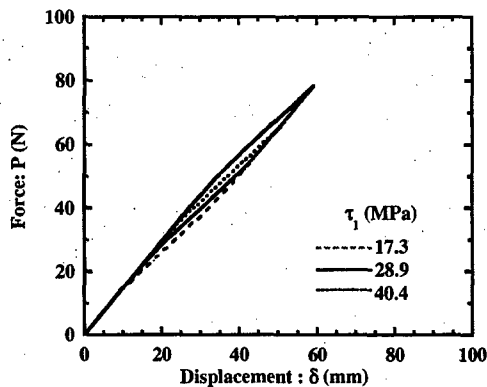
(b) τ_0



(c) G_f

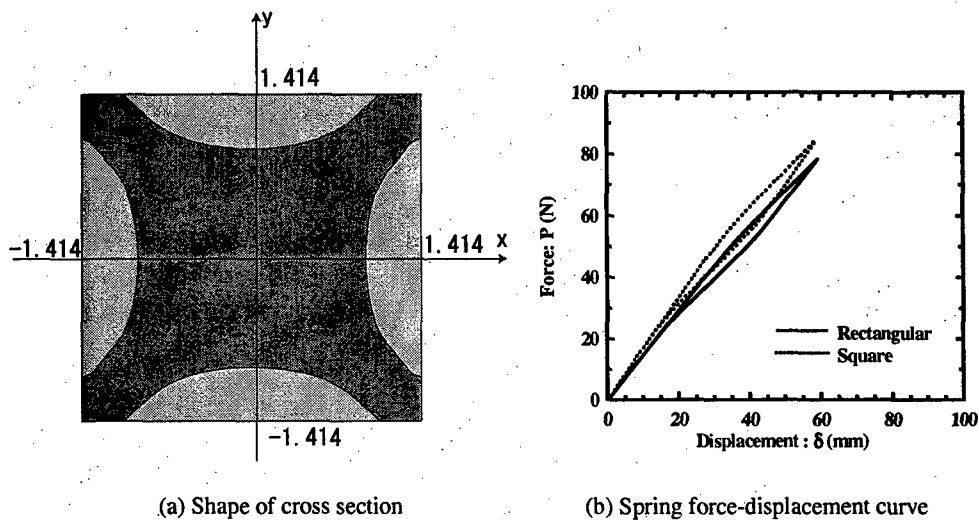


(d) τ_f



(e) τ_1

Figure 15. Effects of various parameters on P- δ relation of FMSA composite springs, (a) SMA shear modulus, G_{SMA} , (b) forward transformation shear stress, τ_0 , (c) shear modulus of a ferromagnetic material, G_f , (d) the yield stress in shear of a ferromagnetic material, τ_f , and (e) reverse transformation shear stress, τ_1 .



(a) Shape of cross section

(b) Spring force-displacement curve

Figure 16 Superelastic behavior of Fe/CuAlMn composites.

Next, we shall compare the mechanical performance (P- δ relation) of a spring between "rectangular" and "square" cross section. To this end, the cross section area of the square is made equal to that of the rectangular studied earlier (Figure 13). The analytical results of the optimum square cross section of FeCoV/CuAlMn composite are shown in Figure 16(a), while the P- δ relation of the FSMA spring with this square cross

section is given in Figure 16(b) as a dashed line where the results of the rectangular cross section are also shown by solid line. A comparison between the square cross section of Figure 16(a) and the rectangular cross section of Figure 12 reveals that the FSMA composite spring with square cross section provides larger force capability than that with the rectangular cross section for the same cross section area. However, the effectiveness of using the spring with the square cross section remains to be determined after its effectiveness of inducing large magnetic force between the neighboring turns of the spring.

2.5. Concluding remarks

The predicted results of the bending moment - curvature of a FSMA composite plate exhibit superelastic behavior of the composite beam while those of the FSMA composite spring with rectangular cross section show also similar superelastic behavior. The above superelastic behavior is the performance required for FSMA composite actuators with high force and displacement capability. The results of the simple model were used effectively for optimization of the cross section geometry of two types of FSMA composite, bending and torsion types.

Chapter 3. Modeling of Effective Magnetic and Mechanical Properties of Fe-NiTi Particulate Composite

In this chapter, we will discuss two models to predict the magnetic properties of FSMA particulate composites, first for magnetic permeability and second for saturation magnetization.

3.1. Composite Magnetic Permeability

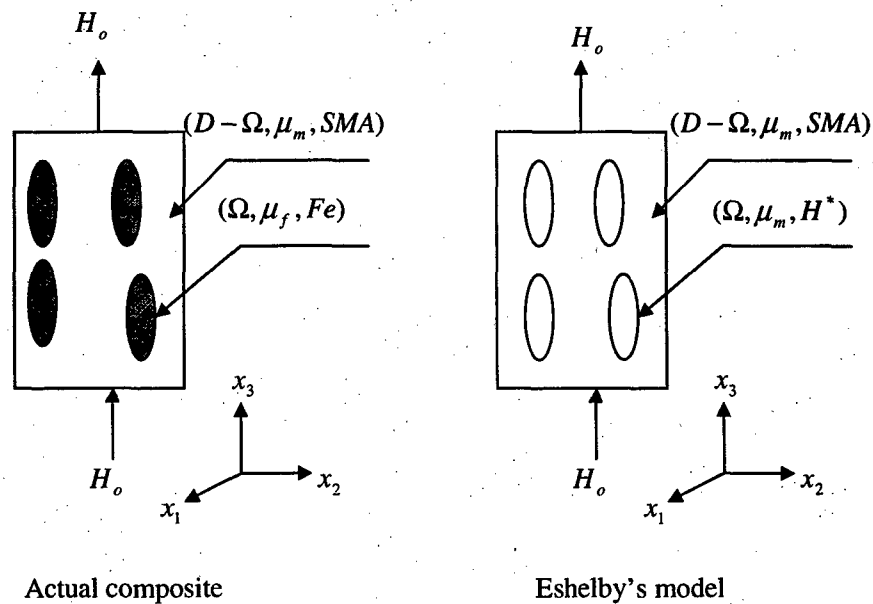


Figure 17. Eshelby's model for a FSMA particulate composite

In the absence of inhomogeneities, see Figure 17,

$$B = \mu_m \cdot H_m \quad (31)$$

Here B is the magnetic flux, H_m is the magnetic field intensity in the matrix and μ_m is the magnetic permeability of the matrix. As shown in figure 17, the matrix phase (m-phase) is the non-ferrous NiTi alloy (paramagnetic material) and Iron in particulate form

constitutes the fiber phase (f-phase). Since the magnetic susceptibility χ for paramagnetic materials typically lies in the range of $10^{-3} - 10^{-5}$, the magnetization vector is very weak.

Therefore, equation (31) takes the following form [12]:-

$$\begin{aligned} H_m &= H_o + M \Leftrightarrow H_m \approx H_o \\ M &\approx 0 \rightarrow \text{Magnetization vector for paramagnetics (NiTi)} \\ \therefore B &= \mu_m \cdot H_o \end{aligned} \quad (32)$$

This error is found to be of the order of 0.01% which is considered acceptable by the PI. Upon addition of inhomogeneity (ferromagnetic phase), the flux and field vectors are related as follows in Ω :-

$$B + B_d = \mu_f \cdot (H_o + H_d) = \mu_m \cdot (H_o + H_d - H^*) \quad (33)$$

By definition for ferromagnetics,

$$B = \mu_o \cdot (H_o + M - N \cdot M) = \mu_f \cdot (H - N \cdot M) \quad (34)$$

where $N \rightarrow$ demagnetization factor, a tensor quantity depending only on the shape of the inhomogeneity, analogous to Eshelby's tensor of mechanical case.

Choosing $H_d = -N \cdot M$ in equation (34) we get,

$$\begin{aligned} H_d &= N \cdot H^* = S^m \cdot H^* \\ \text{or,} \\ B + B_d &= \mu_f \cdot (H_o + S^m \cdot H^*) = \mu_m \cdot (H_o + S^m \cdot H^* - H^*) \\ S^m &= N \text{ "Eshelby's Tensor" for Magnetic case} \end{aligned} \quad (35)$$

From equation (35) H^* can be solved. When the volume fraction of ferromagnetic inhomogeneities (f) becomes finite, the interactions between ferromagnetic particles need to be accounted for. Mori-Tanaka's mean-field theory has been used in the present case¹. We thus define \bar{H} as the average magnetic field and equation (35) gets modified to:-

$$B + B_d = \mu_f \cdot (H_o + \bar{H} + H_d) = \mu_m \cdot (H_o + \bar{H} + H_d - H^*)$$

or, (36)

$$B_d = \mu_m \cdot (\bar{H} + H_d - H^*)$$

Since the volume integration of H_d must vanish over the entire domain, we get,

$$\bar{H} = -f(H_d - H^*)$$
(37)

Substituting in equation (36) and simplifying gives us,

$$H^* = \left[(\mu_f - \mu_m) \cdot \{ (1-f)S^m + fI \} + \mu_m \right]^{-1} \cdot (\mu_m - \mu_f) \cdot H_o$$
(38)

Following the steps enumerated in section 4.2.1 of [13]² the concentration factor tensor A is evaluated,

$$H_f = H_o + \bar{H} + H_d = H_o + H_d(1-f) + fH^* = H_o + \{ (1-f)S^m + fI \} \cdot H^*$$

or, (39)

$$H_f = H_o + \{ (1-f)S^m + fI \} \cdot \left[(\mu_f - \mu_m) \cdot \{ (1-f)S^m + fI \} + \mu_m \right]^{-1} \cdot (\mu_m - \mu_f) \cdot H_o$$

Or,

¹ Atomic interaction effects have been neglected here. This is something that the PI will be considering in future.

² Section on "Effective Property tensor of a composite: Field vector (Z_o) boundary condition"

$$H_f = \left[1 + \{1-f\}S^m + fI \right] \cdot \left[(\mu_f - \mu_m) \cdot \{1-f\}S^m + fI + \mu_m \right]^{-1} \cdot (\mu_m - \mu_f) \cdot H_o$$

or,

$$H_f = A \cdot H_o \quad (40)$$

$$\text{with } A = \left[1 + \{1-f\}S^m + fI \right] \cdot \left[(\mu_f - \mu_m) \cdot \{1-f\}S^m + fI + \mu_m \right]^{-1} \cdot (\mu_m - \mu_f)$$

Thus,

$$\mu_c = \mu_m + f(\mu_f - \mu_m) \cdot A \quad (41)$$

$\mu_c \rightarrow$ Composite magnetic permeability.

Thus, by knowing the properties of the individual constituents of the composite and the geometry of the inclusion, the composite magnetic permeability can be evaluated.

3.2. Saturation Magnetization (M_s^c) of Fe-NiTi particulate composite

The magnetic field intensity in the composite is evaluated as follows³:-

$$\begin{aligned} H_c &= (1-f)\langle H_m \rangle + f\langle H_f \rangle \\ \langle H_f \rangle &= H_o + \bar{H} + H_d \\ &= H_o - f(H_d - H^*) + H_d \\ &= H_o + (1-f)H_d + fH^* \\ \langle H_m \rangle &= H_o + \bar{H} \\ &= H_o - fH_d + fH^* \\ H_c &= H_o + M_s^c \\ &= (1-f)(H_o - fH_d + fH^*) + f(H_o + (1-f)H_d + fH^*) \\ &= H_o + fH^* \\ &= H_o - fM_s \end{aligned} \quad (42)$$

or,

$$M_s^c = fM_s$$

Here, $M_s \rightarrow$ Saturation Magnetization of the ferro - particulate (f - phase)

and $M_s^c \rightarrow$ Composite Saturation Magnetization.

³ $\langle \rangle$ Denotes volume average over the entire domain.

Since the experimental data tabulates the Saturation magnetization for various Fe concentrations, the composite saturation magnetization is a very useful comparison parameter.

We measured the saturation magnetization(M_s) of Fe-TiNi particulate composites that we processed by using Spark Plasma Sintering(SPS), see chapter 4 where four different weight percents of Fe phase are used to form Fe-TiNi composites. We compare the predicted and measured M_s values in Table 1, and also in Figure 18.

Weight % Fe (w)	Volume fraction Fe ⁴ (f)	M_s^c (Experimental)	M_s^c (Predicted)
30	0.26133	40	52.266
50	0.4522	93	90.44
70	0.6582	135	131.64
100	1.0	200	200

Table 1. Comparison of saturation magnetization, M_s between the predictions and experimental data

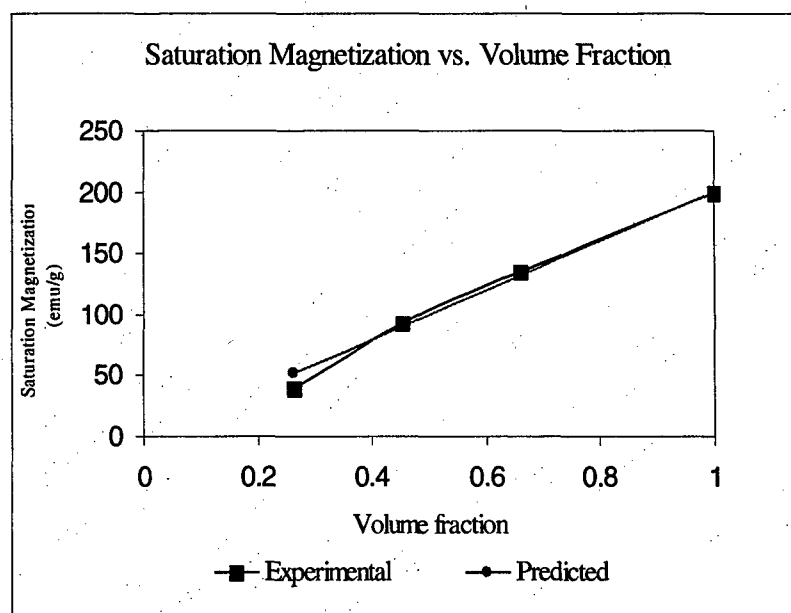


Figure 18. Comparison of saturation magnetization predicted by our model and measured

$$^4 f = \frac{1}{1 + \frac{1-w}{w} \frac{\rho_{Fe}}{\rho_{NiTi}}}; \rho_{Fe}, \rho_{NiTi} \rightarrow \text{densities of Fe and NiTi (7874 and 6500 g/cc respectively)}$$

It is clear by comparing the model predictions and the experimental results that there is not a 100 % match in the values. Especially, for lower volume fractions the model overestimates the Saturation Magnetization of the composite. But the margin of error seems acceptable. The model could be further improved by taking into account the interaction effects which the PI is presently investigating.

3.3. Stiffness properties of a FSMA composite

Here we constructed an analytical model to predict the effective stiffness and slope of the stress-strain (SS) curve of a FSMA particulate composite which is composed of the particulate SMA phase and ferromagnetic matrix phase. The model is restricted to particulate geometry, and also the role of particulate and matrix can be exchanged. The model is based on Eshelby's model. A typical SS curve of a composite containing SMA phase is idealized as in Fig.19 which consists of three linearized stages, the first stage (100% austenite phase, E_A^{NiTi}), second stage a mixture of austenite and martensite phases (E^{NiTi}) and the third stage (100% martensite phase, E_M^{NiTi}). Please note that in the second stage, the fraction of martensite phase increases with increase in stress, thus this stage is often called "stress-induced-martensite phase transformation (SIM)". SIM is a key part of superelastic behavior, shown as the loop in Fig.19. In the following, we state in details the sequence of our model calculations.

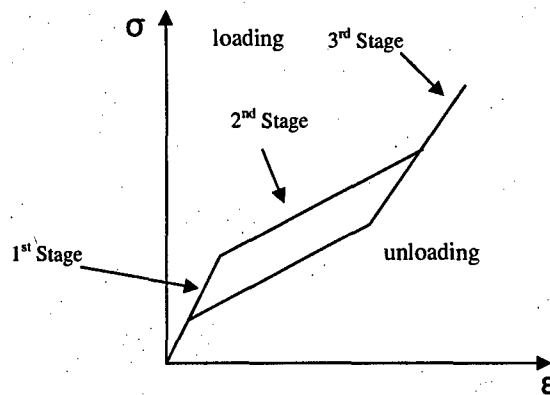


Figure 19. Linearized version of SS Curve of a SMA composite where the first and the third stages are 100% austenite and 100% martensite phase respectively, and the second stage is a mixture of both phases, i.e. stress-induced martensite phase transformation (superelastic stage)

a) 1st stage loading curve

For the first stage of the loading curve, the transformation strain $\epsilon_T = \mathbf{0}$. The problem thus reduces to Eshelby's inhomogeneity problem (Figure 20) where the applied stress causes a relative strain among the matrix and fiber. Using Mori-Tanaka's Mean Field Theory in association with Eshelby's the stresses in the fiber Ω domain are given by:-

$$\sigma^o + \sigma = E^{NiTi} \cdot (\epsilon^o + \bar{\epsilon} + \epsilon) = E^{Fe} \cdot (\epsilon^o + \bar{\epsilon} + \epsilon - \epsilon^*) \quad (43)$$

Here,

$\sigma^o \rightarrow$ applied stress field

$\sigma \rightarrow$ disturbance stress field

$\epsilon \rightarrow$ disturbance strain field

$\bar{\epsilon} \rightarrow$ average strain due to interactions

$E^{Fe} \rightarrow$ stiffness tensor of Fe

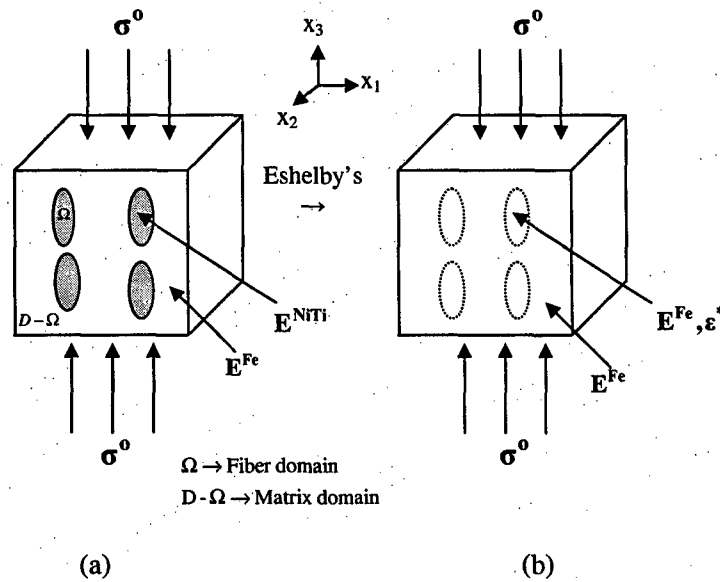


Figure 20. Eshelby's Inclusion problem for use in the simulation of first and third stages behavior in SS curve of a SMA composite

By definition,

$$\boldsymbol{\varepsilon}^o = (\mathbf{E}^{Fe})^{-1} \cdot \boldsymbol{\sigma}^o \quad (44)$$

or,

$$\boldsymbol{\sigma} = \mathbf{E}^{Fe} \cdot (\bar{\boldsymbol{\varepsilon}} + \boldsymbol{\varepsilon} - \boldsymbol{\varepsilon}^*) \quad (45)$$

The volume average strain disturbance over the entire domain is zero, thus we get:-

$$\bar{\boldsymbol{\varepsilon}} = -f(\boldsymbol{\varepsilon} - \boldsymbol{\varepsilon}^*) \quad (46)$$

Substituting equation (46) in (43) and after some algebra we get:-

$$\mathbf{E}_c = \left[(\mathbf{E}^{Fe})^{-1} + f\mathbf{K} \right]^{-1} \quad (47)$$

where

$$\boldsymbol{\varepsilon}^* = \mathbf{K} \cdot \boldsymbol{\sigma}^o$$

$$\mathbf{K} = \left[(\mathbf{E}^{NiTi} - \mathbf{E}^{Fe}) \cdot ((1-f)\mathbf{S} + f\mathbf{I}) + \mathbf{E}^{Fe} \right]^{-1} \cdot (\mathbf{E}^{Fe} - \mathbf{E}^{NiTi}) \cdot (\mathbf{E}^{Fe})^{-1} \quad (48)$$

and where

$$\mathbf{E}^{NiTi} \rightarrow \mathbf{E}_A^{NiTi}, \text{ during stage 1 loading and } \mathbf{E}^{NiTi} \rightarrow \mathbf{E}_M^{NiTi}, \text{ during stage 3 loading}$$

Calculation of σ_{Ms}^c

From equation (47) we can find the slope of the compression SS curve of the composite given the input parameters, namely, material properties of constituent phases NiTi and Fe. But in order to trace the SS curve of the composite, we need to evaluate the stress required to be applied to the specimen such that the NiTi phase of the composite has a stress value equal to Martensite Start Stress (σ_{Ms}^{NiTi}). The following set of equations describes a way of doing that:-

$$\sigma_{Ms}^c = \sigma^o = V_o \sigma_{33} = (1-f)\sigma^{Fe} + f\sigma_{Ms}^{NiTi} \quad (49)$$

$$\sigma^{Fe} = (\mathbf{I} - f\mathbf{E}^{Fe} \cdot (\mathbf{S} - \mathbf{I}) \cdot \mathbf{K}_A) \cdot \boldsymbol{\sigma}^o \Rightarrow \sigma^{Fe} = \mathbf{RA} \cdot \boldsymbol{\sigma}^o \quad (50)$$

where

$$\mathbf{V}_o = [001000]^T; \mathbf{RA} = (\mathbf{I} - \mathbf{E}^{Fe} \cdot f(\mathbf{S} - \mathbf{I}) \cdot \mathbf{K}_A); \quad (51)$$

$$\mathbf{K}_A = \left[(\mathbf{E}_A^{NiTi} - \mathbf{E}^{Fe}) \cdot \{(1-f)\mathbf{S} + f\mathbf{I}\} + \mathbf{E}^{Fe} \right]^{-1} \cdot (\mathbf{E}^{Fe} - \mathbf{E}_A^{NiTi}) \cdot (\mathbf{E}^{Fe})^{-1} \quad (52)$$

$$\Rightarrow (\mathbf{I} - \mathbf{R}\mathbf{A})\mathbf{V}_0\sigma_{33} = f\sigma_{Ms}^{NiTi}; \mathbf{R}\mathbf{A}\mathbf{B} = (\mathbf{I} - \mathbf{R}\mathbf{A})\mathbf{V}_0 \Rightarrow \sigma_{33} = \frac{f\sigma_{Ms}^{NiTi}(3,1)}{\mathbf{R}\mathbf{A}\mathbf{B}(3,1)} \quad (53)$$

Thus, applying σ_{33} stress in 3-direction would produce SIM in the NiTi phase of the FSMA composite. Similarly, the total strain in the composite is given by:-

$$\begin{aligned} \langle \boldsymbol{\varepsilon} \rangle_{total} &= (1-f)\langle \boldsymbol{\varepsilon} \rangle_{Fe} + f\langle \boldsymbol{\varepsilon} \rangle_{NiTi} \Rightarrow \langle \boldsymbol{\varepsilon} \rangle_{total} = (1-f)(\boldsymbol{\varepsilon}^0 + \bar{\boldsymbol{\varepsilon}}) + f(\boldsymbol{\varepsilon}^0 + \bar{\boldsymbol{\varepsilon}} + \boldsymbol{\varepsilon}) \\ \Rightarrow \langle \boldsymbol{\varepsilon} \rangle_{total} &= \boldsymbol{\varepsilon}^0 + f\boldsymbol{\varepsilon}^* \Rightarrow \langle \boldsymbol{\varepsilon} \rangle_{total} = \left[(\mathbf{E}^{Fe})^{-1} + f\mathbf{K}_A \right] \cdot \boldsymbol{\sigma}^0 = \left[(\mathbf{E}^{Fe})^{-1} + f\mathbf{K}_A \right] \cdot \mathbf{V}_0\sigma_{33} \end{aligned} \quad (54)$$

Thus, the point $(\sigma_{33}, \langle \boldsymbol{\varepsilon} \rangle_{total}(3,1))$ indicates the first "kink" point of the assumed linear SS curve of the FSMA particulate composite.

b) 2nd stage loading curve

In the second stage of loading, an eigenstrain $\boldsymbol{\varepsilon}^T$, phase transformation strain from Austenite to Martensite, exists in the NiTi fiber region. Since the eigen strain or the non-elastic strain exists only in the fiber phase, the problem is identical to Eshelby's inhomogeneity inclusion problem (Figure 21). This can be represented as follows:-

$$\text{In } \Omega, \mathbf{E}_{AM}^{NiTi} \cdot (\boldsymbol{\varepsilon}^0 + \bar{\boldsymbol{\varepsilon}} + \boldsymbol{\varepsilon} - \boldsymbol{\varepsilon}^T) = \mathbf{E}^{Fe} \cdot (\boldsymbol{\varepsilon}^0 + \bar{\boldsymbol{\varepsilon}} + \boldsymbol{\varepsilon} - \boldsymbol{\varepsilon}^T - \boldsymbol{\varepsilon}^*) = \mathbf{E}^{Fe} \cdot (\boldsymbol{\varepsilon}^0 + \bar{\boldsymbol{\varepsilon}} + \boldsymbol{\varepsilon} - \boldsymbol{\varepsilon}^{**}) \quad (55)$$

where

$$\boldsymbol{\varepsilon}^{**} = \boldsymbol{\varepsilon}^* + \boldsymbol{\varepsilon}^T, \boldsymbol{\varepsilon}^T = [-\nu_{NiTi} \quad -\nu_{NiTi} \quad 1 \quad 0 \quad 0 \quad 0]^T \cdot \boldsymbol{\varepsilon}_{33}^T$$

$$\boldsymbol{\varepsilon}^{**} = \mathbf{V} \cdot \boldsymbol{\sigma}^0 + \mathbf{W} \cdot \boldsymbol{\varepsilon}^T$$

$$\mathbf{V} = \left[(\mathbf{E}_{AM}^{NiTi} - \mathbf{E}^{Fe}) \cdot \{(1-f)\mathbf{S} + f\mathbf{I}\} + \mathbf{E}^{Fe} \right]^{-1} \cdot (\mathbf{E}^{Fe} - \mathbf{E}_{AM}^{NiTi}) \cdot (\mathbf{E}^{Fe})^{-1} \quad (56)$$

$$\mathbf{W} = \left[(\mathbf{E}_{AM}^{NiTi} - \mathbf{E}^{Fe}) \cdot \{(1-f)\mathbf{S} + f\mathbf{I}\} + \mathbf{E}^{Fe} \right]^{-1} \cdot \mathbf{E}_{AM}^{NiTi}$$

Since the SS curve of pure NiTi is assumed to be linear, \mathbf{E}_{AM}^{NiTi} , the stiffness tensor of NiTi phase exhibiting $\boldsymbol{\varepsilon}^T$ eigen strain is taken as

$$\mathbf{E}_{AM}^{NiTi}(\boldsymbol{\varepsilon}_{33}^T) = \mathbf{E}_A^{NiTi} + \frac{(\mathbf{E}_M^{NiTi} - \mathbf{E}_A^{NiTi})}{\boldsymbol{\varepsilon}_{total}^T} \cdot \boldsymbol{\varepsilon}_{33}^T \quad (57)$$

where $\boldsymbol{\varepsilon}_{total}^T$ is the total transformation strain during compression loading of NiTi.

The total volume averaged stress in domain D becomes

$$\begin{aligned} \langle \sigma \rangle_D &= \sigma^o = (1-f)E^{Fe} \cdot (\varepsilon^o + \bar{\varepsilon}) + f \langle \sigma \rangle_f \\ \Rightarrow \sigma^o &= (1-f)E^{Fe} \cdot (\varepsilon^o - f(S-I) \cdot \varepsilon^{**}) + f \langle \sigma \rangle_f \\ \Rightarrow \sigma^o &= (1-f)\sigma^o - f(1-f)E^{Fe} \cdot (S-I) \cdot \varepsilon^{**} + f \langle \sigma \rangle_f \\ \Rightarrow [I + (1-f)E^{Fe} \cdot (S-I) \cdot V] \cdot \sigma^o + (1-f)E^{Fe} \cdot (S-I) \cdot W \cdot \varepsilon^T &= \langle \sigma \rangle_f \end{aligned}$$

$$\Rightarrow \begin{bmatrix} 0 \\ 0 \\ 0 \\ 0 \\ 0 \\ 0 \end{bmatrix} \sigma_{33} + (1-f)E^{Fe} \cdot (S-I) \cdot W \cdot \begin{bmatrix} -V_{NTi} \\ -V_{NTi} \\ 1 \\ 0 \\ 0 \\ 0 \end{bmatrix} \varepsilon_{33}^T = \langle \sigma \rangle_f \quad (58)$$

$$\Rightarrow R(6,1)\sigma_{33} + T(6,1)\varepsilon_{33}^T = \langle \sigma \rangle_f$$

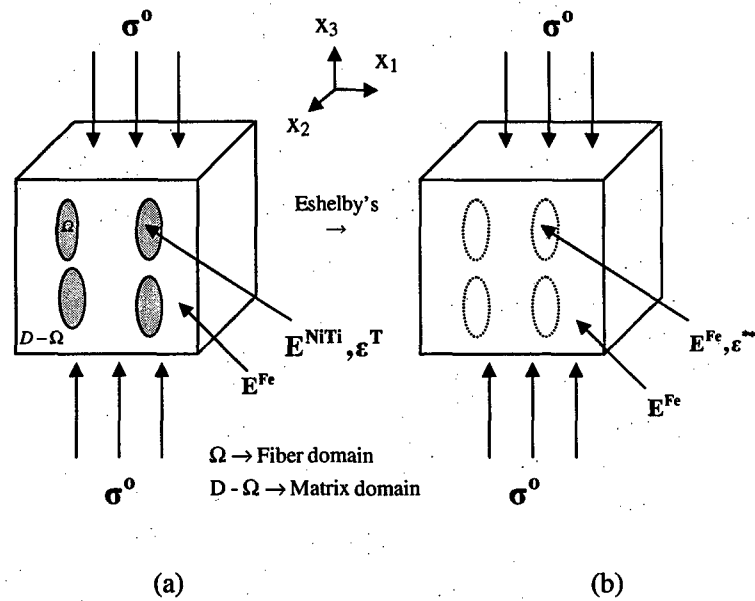


Figure 7. Eshelby's Inhomogeneity Inclusion problem for use in the simulation of the second stage behavior of SS curve of a SMA composite.

$$\Rightarrow R(3,1)\sigma_{33} + T(3,1)\epsilon_{33}^T = \langle \sigma_{33} \rangle_f \Rightarrow \sigma_{33} = \frac{\langle \sigma_{33} \rangle_f - T(3,1)\epsilon_{33}^T}{R(3,1)} \quad (59)$$

where

$$\mathbf{R} = [\mathbf{I} + (1-f)\mathbf{E}^{\text{Fe}} \cdot (\mathbf{S} - \mathbf{I}) \cdot \mathbf{V}] \cdot \begin{bmatrix} 0 \\ 0 \\ 1 \\ 0 \\ 0 \\ 0 \end{bmatrix} \text{ and } \mathbf{T} = (1-f)\mathbf{E}^{\text{Fe}} \cdot (\mathbf{S} - \mathbf{I}) \cdot \mathbf{W} \cdot \begin{bmatrix} -V_{\text{NiTi}} \\ -V_{\text{NiTi}} \\ 1 \\ 0 \\ 0 \\ 0 \end{bmatrix}$$

The volume averaged strain is computed as:-

$$\begin{aligned} \langle \boldsymbol{\epsilon} \rangle_{\text{D}} &= (1-f)(\boldsymbol{\epsilon}^{\circ} + \bar{\boldsymbol{\epsilon}}) + f(\boldsymbol{\epsilon}^{\circ} + \bar{\boldsymbol{\epsilon}} + \boldsymbol{\epsilon} - \boldsymbol{\epsilon}^{\text{T}}) = \boldsymbol{\epsilon}^{\circ} + f(\boldsymbol{\epsilon}^{**} - \boldsymbol{\epsilon}^{\text{T}}) \\ \Rightarrow \langle \boldsymbol{\epsilon} \rangle_{\text{D}} &= ((\mathbf{E}^{\text{Fe}})^{-1} + f\mathbf{V}) \cdot \boldsymbol{\sigma}^{\circ} + f(\mathbf{W} - \mathbf{I}) \cdot \boldsymbol{\epsilon}^{\text{T}} \end{aligned} \quad (60)$$

where

$$\boldsymbol{\sigma}^{\circ} = \begin{bmatrix} 0 \\ 0 \\ 1 \\ 0 \\ 0 \\ 0 \end{bmatrix} \sigma_{33}, \boldsymbol{\epsilon}^{\text{T}} = \begin{bmatrix} -V_{\text{NiTi}} \\ -V_{\text{NiTi}} \\ 1 \\ 0 \\ 0 \\ 0 \end{bmatrix} \epsilon_{33}^T \quad (61)$$

Thus, the applied stress σ_{33} required to cause any given ϵ_{33}^T transformation strain can be calculated using equation (57). Consequently, the total strain exhibited by the composite for the applied stress can be evaluated using (58). Plotting σ_{33} versus $\langle \boldsymbol{\epsilon} \rangle_{\text{D}}$ (3, 1) values obtained by varying ϵ_{33}^T between $(0, \epsilon_{33}^{\text{T total}})$ gives us the SS curve for the Fe-NiTi. It is to be noted that equation (57) makes use of 'older' ϵ_{33}^T to compute $\mathbf{E}_{\text{AM}}^{\text{NiTi}}(\epsilon_{33}^T)$. An iterative process for the calculation of σ_{33} has been proposed here. ϵ_{33}^T is varied between $(0, \epsilon_{33}^{\text{T total}})$ and at each n^{th} step, $\mathbf{E}_{\text{AM}}^{\text{NiTi}}(\epsilon_{33}^T)$ is calculated using $\epsilon_{33}^T(n-1)^{\text{th}}$. By increasing the number of steps, the error can be minimized. The computations are performed using MATLAB.

c) 3rd stage loading curve

Third stage loading curve is similar to the first stage in the sense that there does not exist any transformation strain in the NiTi phase. Thus, the problem can be solved as Eshelby's inhomogeneity (Figure 20). The first step involves calculation of martensite finish stress σ_{Mf}^c as enumerated overleaf:-

$$\sigma_{Mf}^c = \sigma^o = \sigma_{33} V_o = (1-f)\sigma^{Fe} + f\sigma_{Mf}^{NiTi} \quad (62)$$

$$\sigma^{Fe} = (\mathbf{I} - \mathbf{E}^{Fe} \cdot f(\mathbf{S} - \mathbf{I}) \cdot \mathbf{K}_M) \cdot \sigma^o \Rightarrow \sigma^{Fe} = \mathbf{RM} \cdot \sigma^o \quad (63)$$

where

$$V_o = [001000]^T; \mathbf{RM} = (\mathbf{I} - \mathbf{E}^{Fe} \cdot f(\mathbf{S} - \mathbf{I}) \cdot \mathbf{K}_M); \quad (64)$$

$$\mathbf{K}_M = [(\mathbf{E}_M^{NiTi} - \mathbf{E}^{Fe}) \cdot \{(1-f)\mathbf{S} + f\mathbf{I}\} + \mathbf{E}^{Fe}]^{-1} \cdot (\mathbf{E}^{Fe} - \mathbf{E}_M^{NiTi}) \cdot (\mathbf{E}^{Fe})^{-1} \quad (65)$$

$$\Rightarrow (\mathbf{I} - \mathbf{RM})V_o\sigma_{33} = f\sigma_{Mf}^{NiTi}; \mathbf{RMB} = (\mathbf{I} - \mathbf{RM})V_o \Rightarrow \sigma_{33} = \frac{f\sigma_{Mf}^{NiTi}(3,1)}{\mathbf{RMB}(3,1)} \quad (66)$$

Thus, applying σ_{33} stress in 3-direction would produce $\sigma_{Mf}^{NiTi}(3,1)$ in NiTi phase of the FSMA composite.

The total strain in the composite is given by:-

$$\begin{aligned} \langle \epsilon \rangle_{total} &= (1-f)\langle \epsilon \rangle_{Fe} + f\langle \epsilon \rangle_{NiTi} \Rightarrow \langle \epsilon \rangle_{total} = (1-f)(\epsilon^o + \bar{\epsilon}) + f(\epsilon^o + \bar{\epsilon} + \epsilon) \\ \Rightarrow \langle \epsilon \rangle_{total} &= \epsilon^o + f\bar{\epsilon} \Rightarrow \langle \epsilon \rangle_{total} = [(\mathbf{E}^{Fe})^{-1} + f\mathbf{K}_M] \cdot \sigma^o = [(\mathbf{E}^{Fe})^{-1} + f\mathbf{K}_M] \cdot V_o\sigma_{33} \end{aligned} \quad (67)$$

Thus, the point ($\sigma_{33}, \langle \epsilon \rangle_{total}(3,1)$) indicates the second "kink" point of the assumed linear SS curve of the FSMA particulate composite.

Chapter 4. Processing of Particulate FSMA Composites

One of the proposed FSMA composite in the present work is a “particulate composite” composed of particulate powders of SMA (NiTi) of superelastic (SE) grade and ferromagnetic material, i.e., soft iron (Fe). The ordinary metallurgical route for processing particulate composites using powders i.e., standard sintering with long duration of high temperature produces unwanted reaction products destroying the original properties of SMA and ferromagnetic material. Therefore, Spark Plasma Sintering (SPS) is applied to a mixture of NiTi-SE and Fe powders in vacuum at various temperatures for a period of 5 minutes. Since University of Washington did not have an SPS system, when this project was started in 2001, the SPS located at Material Processing Department, Tohoku University was accessed. Later, thanks to the DURIP AF grant on equipmental proposal, we were awarded a new DURIP grant by which we purchased a new SPS machine (Sumitomo Coal Mines, Japan, model Dr. Sinter SPS-1020S). Schematic of SPS machine is shown in Figure 22. The interface of the composite is found to be free of inter-metallic compounds which are known to make the composite brittle. Profs. Kang and Kawasaki of Tohoku University, Japan helped us process the FSMA composites used in this early part of the work. Though the current model will also hold true for laminate composites as a special case, particulate FSMA composite is considered due to the superior quality of composite obtained through SPS processing. Particulate NiTi-Fe composites were processed by SPS at 600°C in vacuum for 5 minutes and 50MPa with 30, 50 and 70% Fe by weight. The magnetization (M) – magnetic field (H) curves of the composite specimens are then measured using vibrating specimen magnetometer (VSM), located at Tohoku University, are shown in Figure 20. The saturation magnetization (M_s) taken from Fig. 23 are compared with the model results, Fig. 18, see its details in Chapter 3.

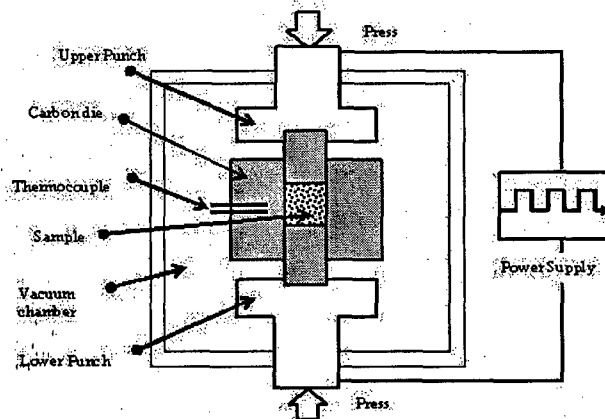


Figure 22. Schematic of Spark Plasma Sintering (SPS) machine used to process FSMA particulate composites.

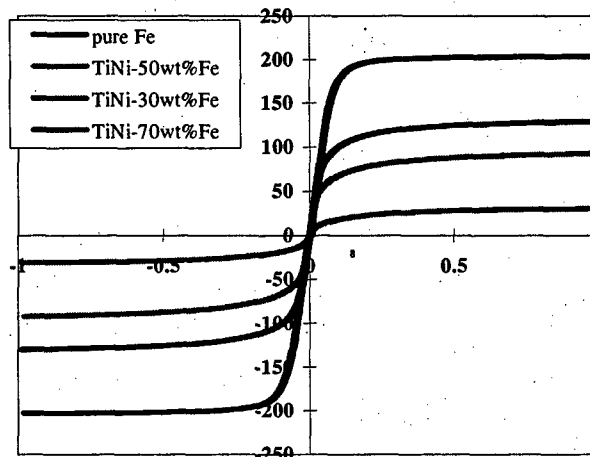
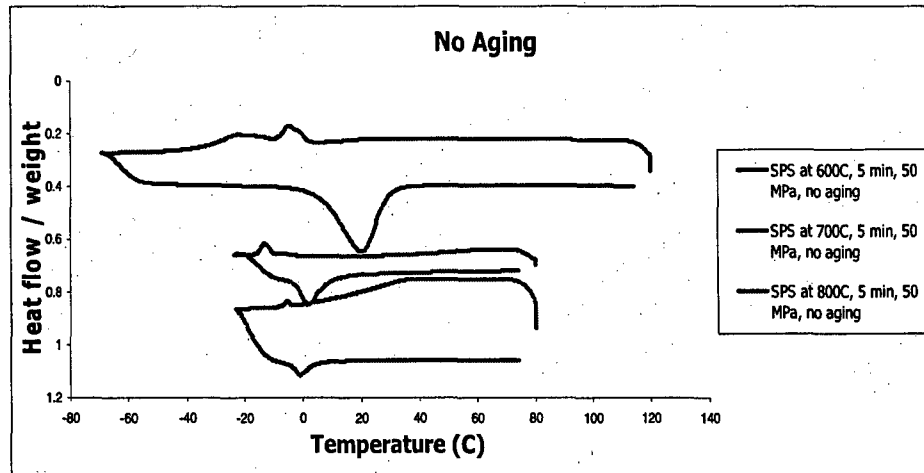


Figure 23. $M(\text{emu/g}) - H(\text{Tesla})$ curves of Fe-TiNi composites processed by SPS and measured by VSM.

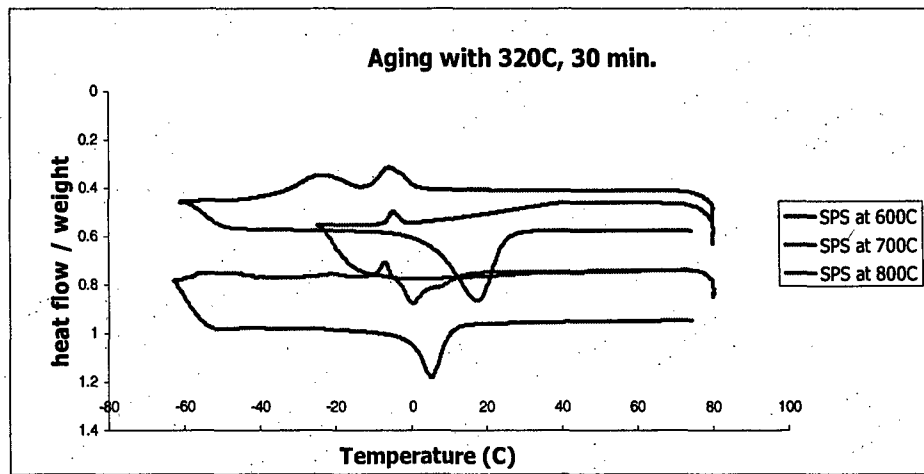
As far as the magnetic behavior of the Fe-TiNi composite is concerned, Figure 23 demonstrates the good magnetic behavior that is predicted by the new model.

We tried several SPS conditions and heat treatments, to identify the best SPS condition (The SPS conditions used are, 600 C, 700 C, and 800 C all under 50 MPa for 5 min, in vacuum).

Figure 24 (a) and (b) show the DSC results of Fe (33.3 %wt average dia=100nm) – TiNi (average dia=212 μ m) with these three different SPS temperatures without and with aging heat treatment of 320 C for 30min.



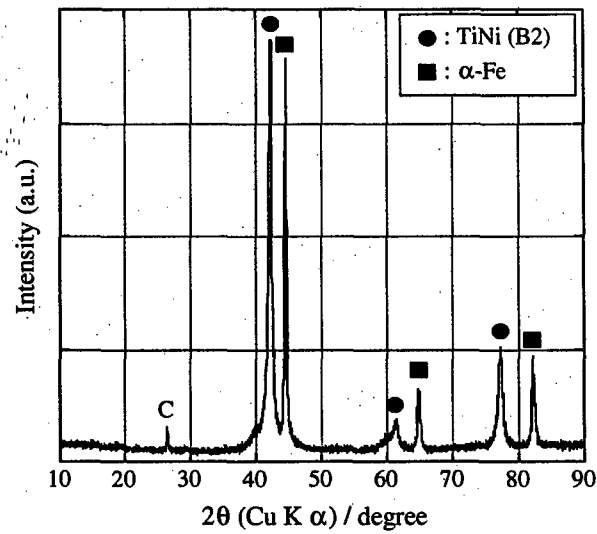
(a) No heat treatment



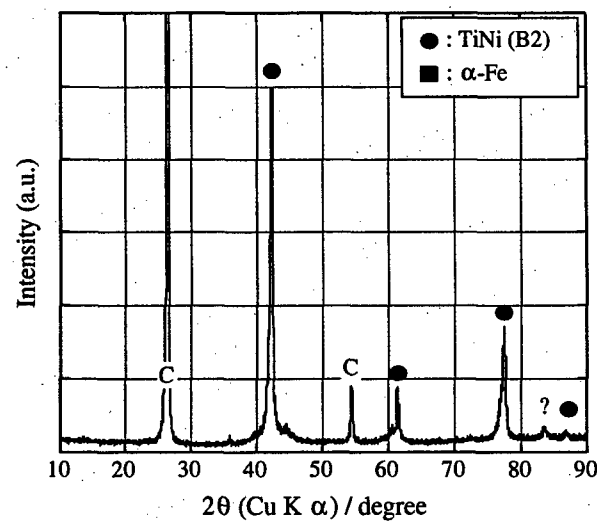
(b) 320 C, 30 min heat treated

Figure 24. Comparison 51at%NiTi (212 microns) + 33.33%wtFe (100 nm) Composite processed using SPS at 600, 700 and 800oC for 5 min, 50 MPa in vacuum.

Figure 24 indicates that the best SPS temperature is 700C, 50 MPa, 5 min in vacuum conditions, and the aging increased the transformation temperatures shown by peaks. XRD analysis of the as-SPS processed with 700 and 900 C were performed and the results are shown in Figure 25 (a) and (b), respectively.



(a) 51at%NiTi (212 μm)+33.33%wtFe (74 μm) composite, SPS at 700oC, 5 min, 50 MPa



(b) 51at%NiTi (212 μm)+33.33%wtFe (74 μm) composite, SPS at 900oC, 5 min, 50 MPa

Figure 25. XRD of the composite NiTi obtained from different SPS processes.

Figure 25 reveals that use of higher temperature for SPS resulted in excess amount of C which presumably came from the graphite mold. Therefore, use of lower temperature is desired. However, lower temperature SPS process resulted in higher porosity in the samples. The effects of SPS temperature on the density of the samples are summarized in Table 2. From the results of Table 2, DSC data of Figure 24 and XRD data of Figure 25, use of 700 °C is considered to be best.

Sample ID SPS°C, 5min, 50 MPa	Density measured*	Theoretical density	Porosity (%)
600°C, 51at%NiTi (212 μm)+33.33%wt Fe (100 nm)	6.66	6.88	3.2
700°C, 51at%NiTi (212 μm)+33.33%wt Fe (100 nm)	6.65	6.88	3.2
800°C, 51at%NiTi (212 μm)+33.33%wt Fe (100 nm)	6.65	6.88	3.2
700°C, 51at%NiTi (212 μm)+33.33%wt Fe (74 μm)	6.56	6.88	4.6
700°C, 51at%NiTi (MRi)+33.33%wt Fe (100 nm)	6.32	6.88	8.1
900°C, pure 51at%NiTi (212 μm) sample	6.26	6.40	2.1
600°C, Dr. Kang's sample	6.07	6.88	11.8

Table 2. Density^o of samples

We also attempted nano-sized TiNi powders which were supplied from Materials Research International (MRi) and Argonide Inc. Figure 26 shows the DSC results of 100% TiNi sample processed by SPS and using nano-TiNi powders (Ti -51 at %Ni) at 850 °C, 5 min, 50 MPa, followed by aging at 320 °C for several different hours. It is obvious from Fig. 26 that all DSC charts did not exhibit any peaks, indicating no phase transformation during heating and cooling curves.

* Using Archimedes Principle
 $\rho_{\text{NiTi}} \rightarrow 6.4 \text{ gm/cm}^3$; $\rho_{\text{Fe}} \rightarrow 7.86 \text{ gm/cm}^3$
^o in gm/cm³

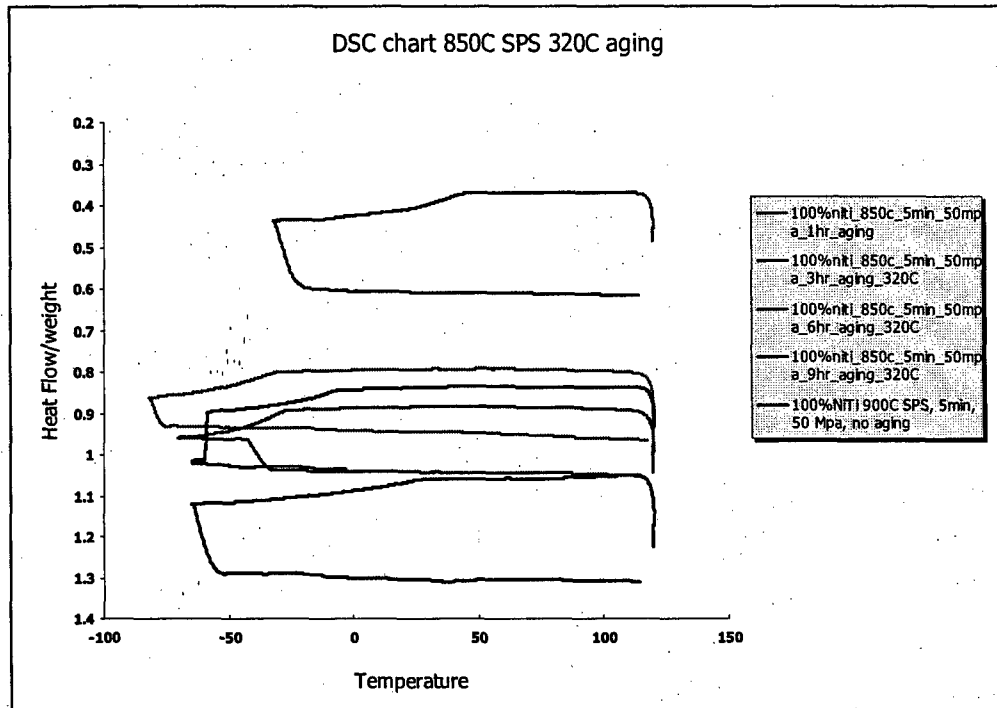


Figure 26. DSC chart of 100% TiNi sample, aging at 320 °C for several different hours

We also Processed 30wt%Fe – nano TiNi (10 nm dia) composite by SPS at 800 °C, for 5 min, under 50 MPa, in vacuum, which was subjected to XRD analysis. The result of XRD analysis of 30wt%Fe – TiNi composites are shown in Figure 27 as open symbol where the XRD result of nano-TiNi powders (Ti -51 at % Ni) are also shown as a reference. Figure 27 indicates the formation of excess amount of TiNi₃ which may have suppressed the formation of TiNi phase, i.e. B2 and B19'. Due to highly reactive nature of the nano-sized TiNi powders, the as-SPS processed Fe-TiNi (MRi) composites did not give rise to any SMA-SE properties.

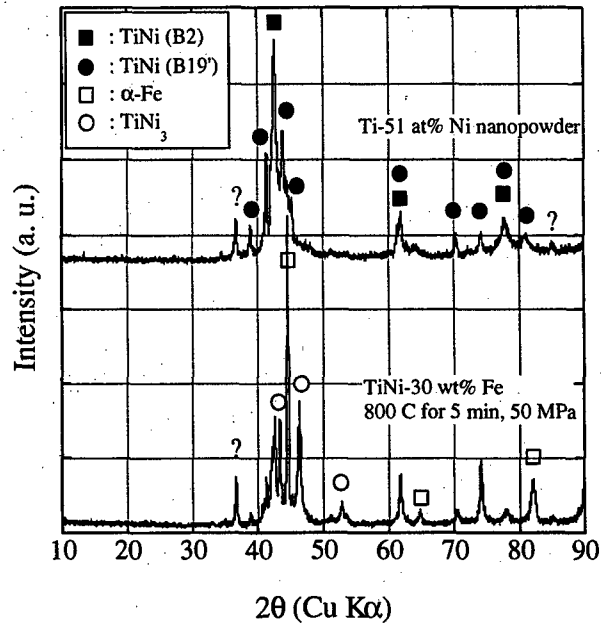


Figure 27. Comparison of XRD results of TiNi nano powder and TiNi/Fe composite

Therefore, we focus only on use of TiNi powders whose average diameter is 212 μm , supplied by Sumitomo Metals, Japan. In the following, all TiNi designation referred to this larger sized TiNi powder (212 μm) as a starting material.

The cross section of as-SPS processed 30 %wt Fe-TiNi composite is taken by SEM with EDAX element analyzer at UW-MSE laboratory, and the results are shown in Fig.28 where (a) , (b) and (c) denote the cross section with three different color coded elements,

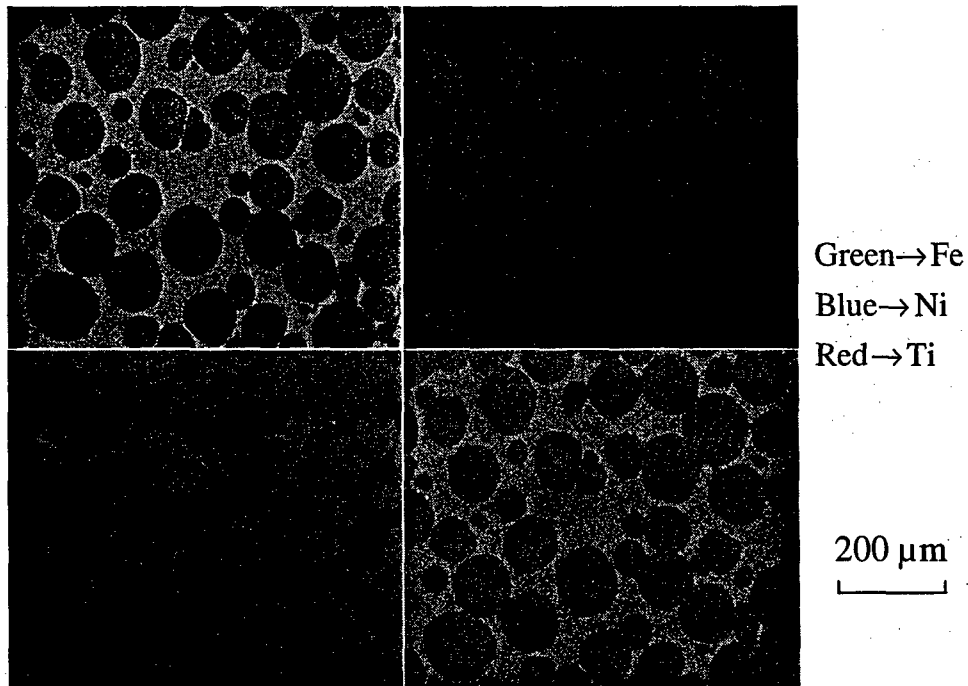


Figure 28. (a) Cross section of Fe (30 wt) - TiNi Composite where particulate phase is TiNi and matrix phase is Fe

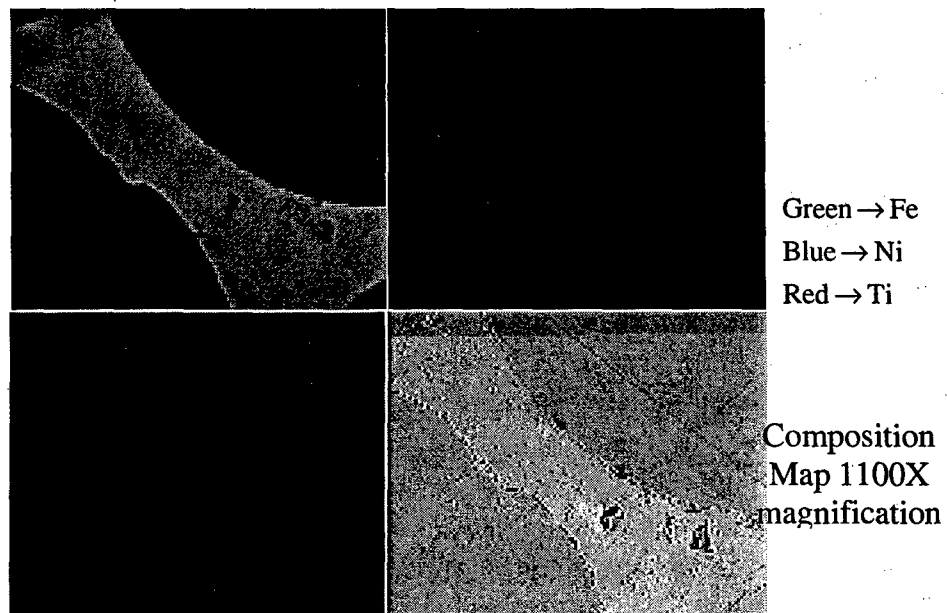
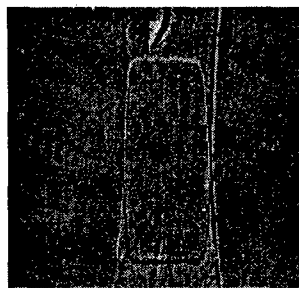
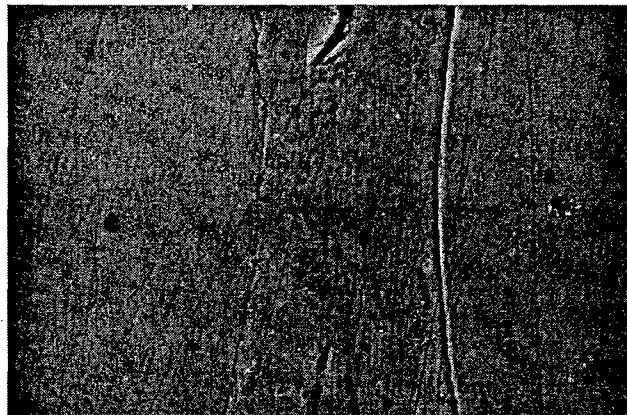


Figure 28. (b) Larger magnification view of the cross section of Fe (30 wt) - TiNi Composite



Line profile at
4300X
Magnification

Figure 28. (c) Line profile of Fe and TiNi phase between two adjacent TiNi particulates.

The Fe (30 %wt) – TiNi (ave. dia = 212 μ m) composites that are processed by SPS with 700 °C, 5 min. 50 MPa in vacuum are subjected to compression testing at different testing temperatures. The results of compressive stress-strain (SS) curves are shown in Figure 29 where (a), (b), (c) correspond to the SS curves tested 41°C, -4°C, -20°C, respectively. The SS curves tested at higher temperature show superelastic (SE) behavior, while the SS curves at lower temperature exhibit shape memory effect (SME) behavior. This is due to the fact that $A_f= 40$ °C, $A_s= -10$ °C, $M_s= -30$ °C, $M_f= -50$ °C, as shown in the DSC chart, see Figure 29 (d).

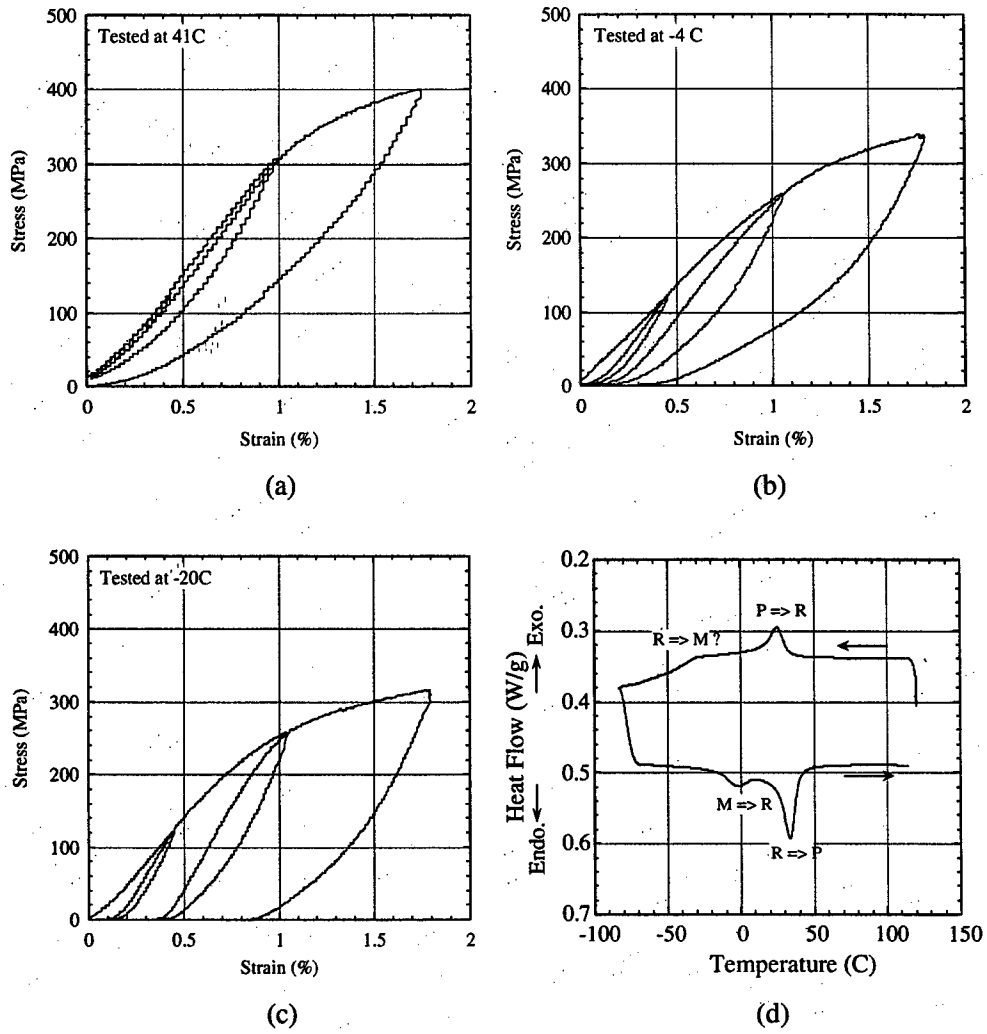


Figure 29. Changes in S-S Curve at Various Temperatures in TiNi / Fe Composite

Chapter 5. Processing of FSMA Laminated Composites by Plasma Etching/Cladding Method

Once the optimum microstructure of a FSMA composite is identified by the above modeling, the next key step in the current AFOSR research is processing of such a FSMA composite. During the past several years, we attempted the processing of FSMA laminated composites by plasma-etching and cladding method where three kinds of FSMA composite material systems are focused on:

- (1) TiNi-FeCoV with Al as adhesive layer
- (2) TiNi-FeCoV with Ag as adhesive layer
- (3) CuAlMn-Fe with Mo as adhesive layer

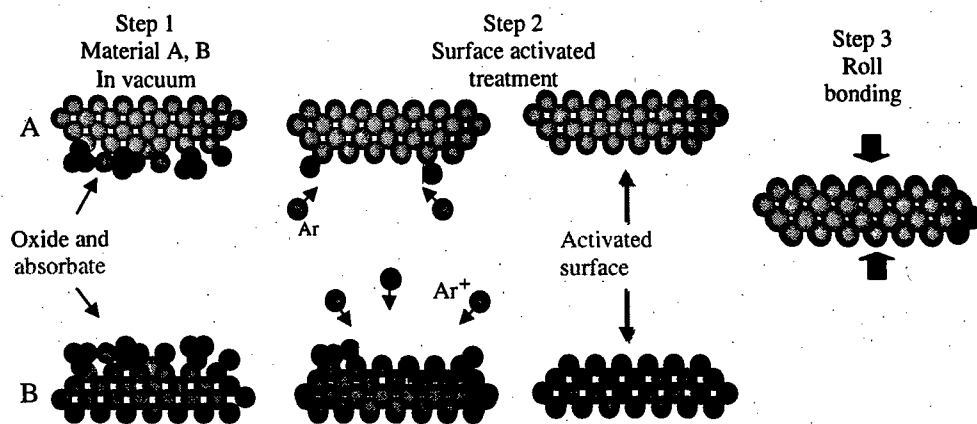


Figure 30. Schematic of plasma-etching/cladding process (Taya, 2005).

The processing of a FSMA laminated composite by the plasma-etching/cladding in vacuum was performed by the facility at Toyo Kohan Co. Ltd., Japan as this company has such equipment. The concept of the plasma-etching/cladding is shown in Figure 30. The plasma-etching/cladding has been successfully applied to the bonding of two thin metal plates for use in electronic packaging applications (Taya, 2005). However, the order of the thicknesses of ferromagnetic plate (FeCoV in the first attempt) and SMA-SE plate (TiNi) is 0.2-1 mm range. Therefore, we have to use an adhesive thin metal foil to

bond these metal plates after heating to 500 °C range. The cross section of the above composite plate is shown in Fig. 31 where thin aluminum layer was used as adhesive material.

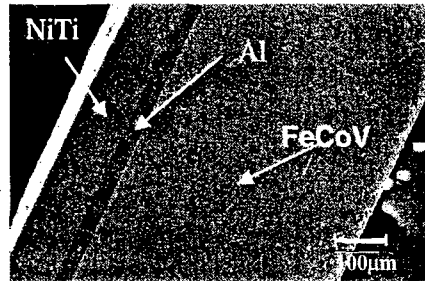
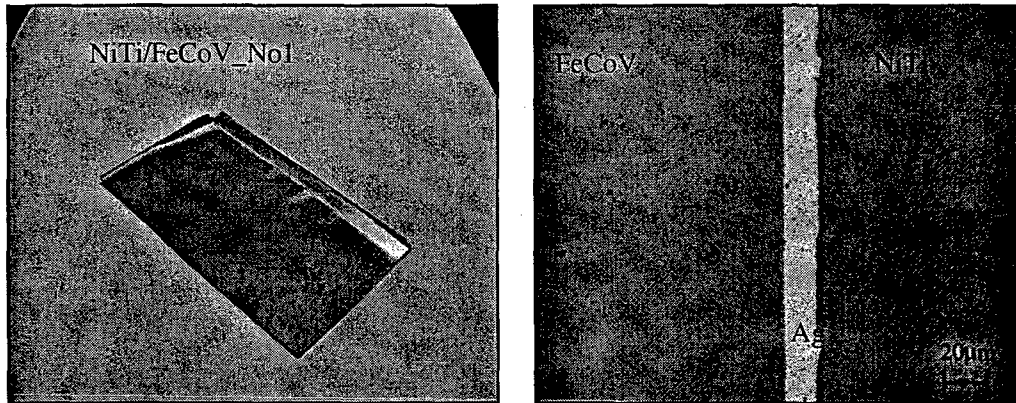


Figure 31. Cross section view of FSMA composite made of NiTi (SME-SE) and FeCoV(ferromagnetic material) with aluminum adhesive layer, processed by plasma-etching/cold rolling process.

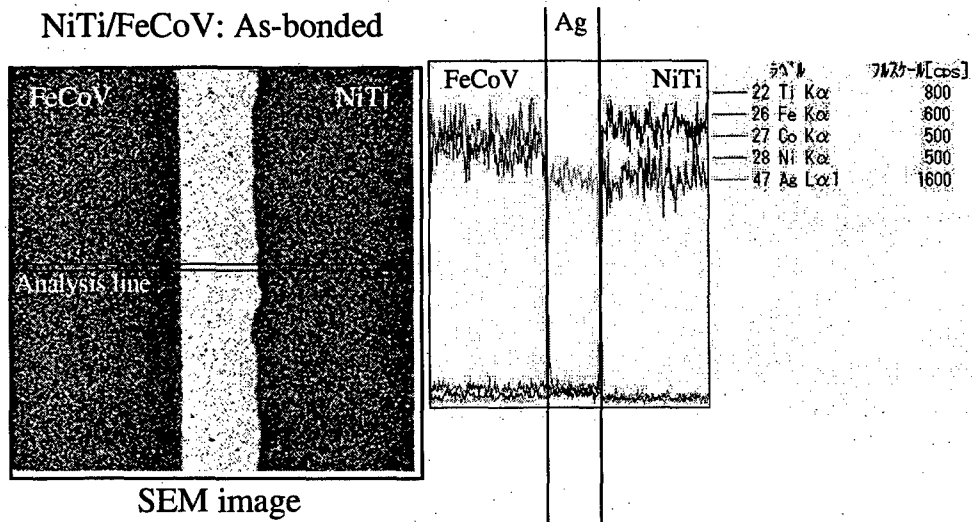
It is noted in the design of FSMA composite of Fig. 31 that use of FeCoV is advantageous as a soft magnetic material because its saturation magnetization (M_s) is as high as 2.2 T. However, to make FeCoV converted to such a high performance soft ferromagnetic grade, we have to apply high temperature heat treatment in H_2 environment while intermediate heat treatment is required of TiNi to convert it to SE grade in air. Thus, we have to make a good compromise in selecting a combined heat treatment to be applied to FeCoV/TiNi composite.

In order to improve the high temperature stability of TiNi/FeCoV composite, we applied Ag thin adhesive layer instead of Al for bonding of TiNi and FeCoV plates as Ag can sustain higher temperature than Al during the past heat treatments. Fig. 32 shows as-bonded NiTi/Ag/FeCoV composite where (a), (b) denote the overview, cross section of the composite plate, respectively and (c) exhibits the EDX analysis of NiTi/FeCoV sheet composite. DSC measurements and B-H curve of this composite after it was heat-treated (800°C 30min in vacuum, water quenched) are shown in Fig. 33 (a) and (b). Fig. 33 indicates that the NiTi/FeCoV FSMA composite processed by the plasma etching/diffusion bonding with Ag layer exhibits phase transformation under temperature change and reasonably good magnetization (M) vs. magnetic field (H) relation.



(a) Overview

(b) Cross section



(c) EDX analysis of NiTi/FeCoV Sheet Composite,
There are no inclusions, compounds at interface.

Figure 32. TiNi/FeCoV FSMA composite plate where adhesive thin Ag layer was used for firm bonding.

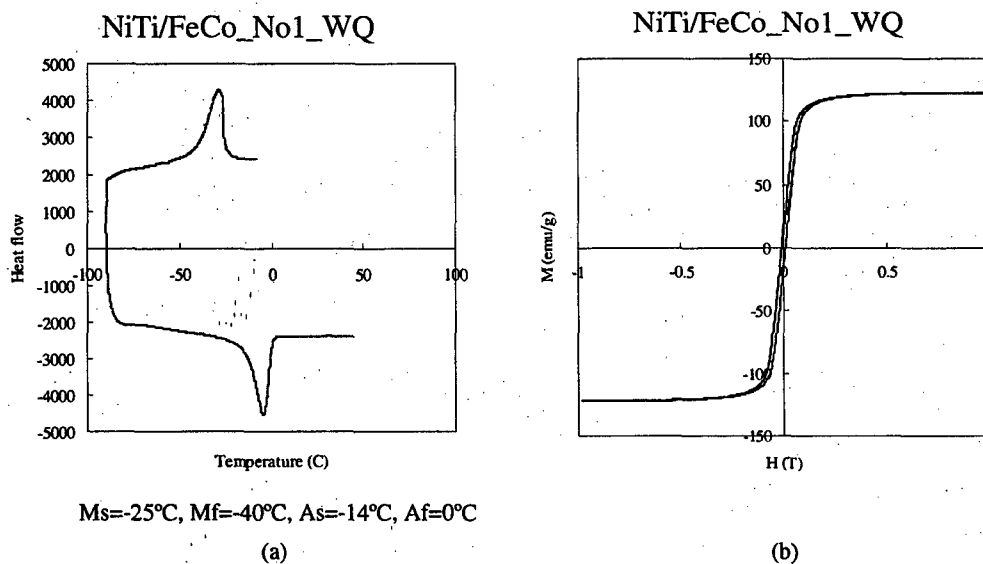


Figure 33. (a) DSC data, (b) M-H curve of TiNi/FeCoV composite.

Finally we attempt to process CuAlMn-Fe laminated composites by plasma-etching cladding method where Mo was used as adhesive layer. Figure 34 (a), (b) and (c) show as-bounded composite, the cross section of CuAlMn(bottom)-Mo(middle)-Fe(top), at low and higher magnifications, respectively. This figure indicates strong bounding between them.

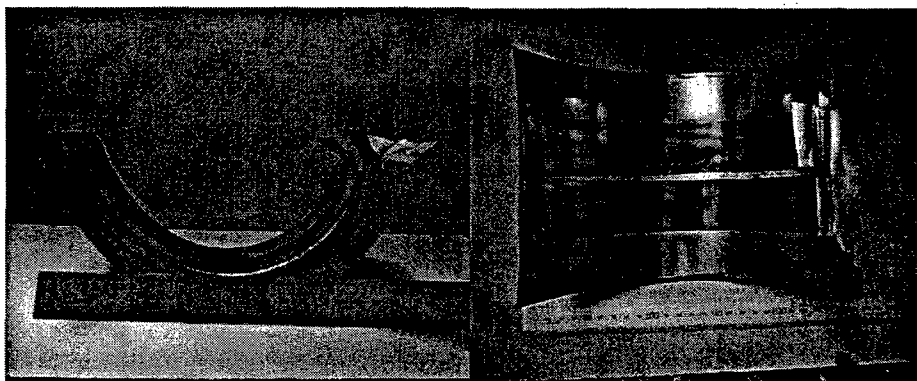
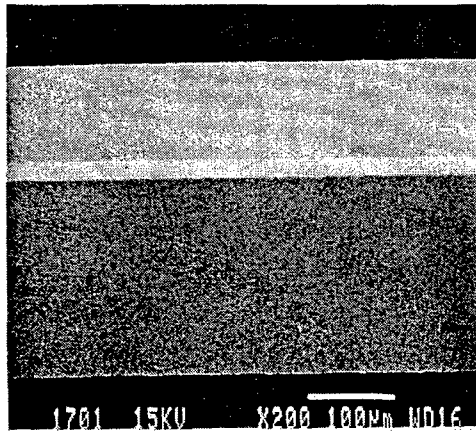
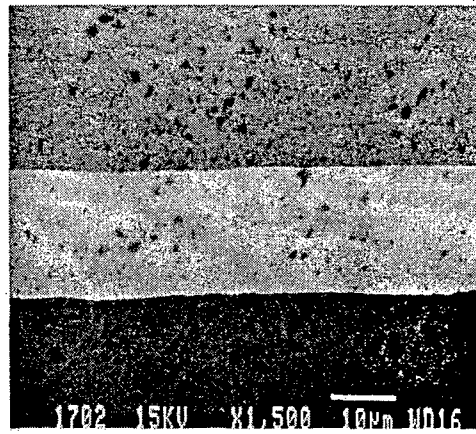


Figure 34. (a) Appearance of CuAlMn/Fe as-cladded and heat-treated



(b)



(c)

Figure 34. Cross section of CuAlMn/Mo/Fe composite (b) entire thickness
(c) magnified view of the interfaced area

References

- [1] T. Sohmura, R. Oshima and F.E. Fujita, *Scripta Metallurgica*, 14 (1980) 855-856.
- [2] R. D. James and M. Wuttig, *Philosophical Magazine A*, 77 (1998) 1273-1299.
- [3] Y. Liang, H. Kato and M. Taya, *Proc. Plasticity '00: 8th Int. Symp. on Plasticity and Current Applications*, 193 (2000).
- [4] Y. Liang, H. Kato, M. Taya and T. Mori, *Scripta Mat.*, 45 (2001) 569.
- [5] S. J. Murray, M. Frinelli, C. Kantner, J. K. Huang, S. M. Allen and R. C. O'Handley, *Journal of Applied Physics*, 83 (1998) 7297.
- [6] R. D. James, R. Tickle and M. Wuttig, *Materials Science and Engineering A*, 273 (1999) 320.
- [7] K. Ullakko, J. K. Huang, V. V. Kokorin and R. C. O'Handley, *Scripta Materialia*, 36 (1997) 1133.
- [8] H. Kato, T. Wada, T. Tagawa, Y. Liang and M. Taya, *Proc. of 50th Anni. of Japan Society of Mater. Sci., Osaka, May 21-26, (2001)* 296.
- [9] T. Yamamoto, M. Taya, Y. Sutou, Y. Liang, T. Wada and L. Sorrenson, *Acta Mater.*, 52(2004), 5083.
- [10] M.Kusaka and M.Taya. (2004) *Journal of Composite Materials*. Vol. 38, No. 12: 1011-1035.
- [11] S.P. Timoshenko and J.N. Goodier, *Theory of Elasticity*, 3rd edition, McGraw-Hill, New York, (1970),
- [12] S.Chikazumi, *Physics of Magnetism*, (1964) John Wiley & Sons.
- [13] M. Taya, *Electronic Composites*, (2005), Cambridge University

Appendix A: Relation Between Bending Moment and Curvature for Laminated Composites

The relation between the normalized bending moment and the normalized curvature of the FMSA composite plate is classified into the following eight patterns as shown Figure A.1.

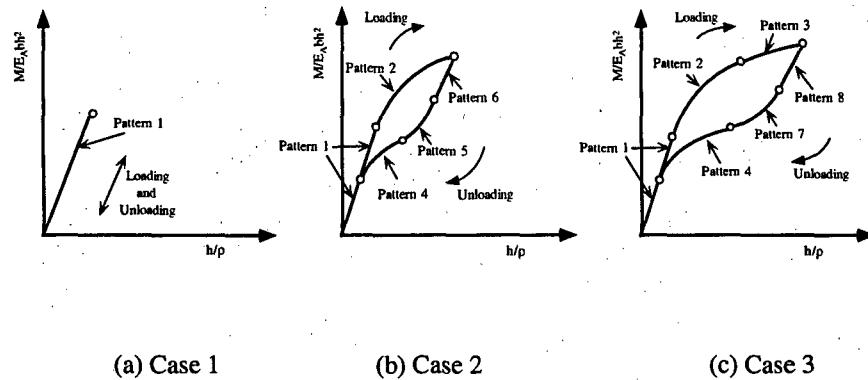


Figure A.1 Relation between Normalized Bending Moment and Normalized curvature.

Case 1 is constructed with only Pattern 1 (Figure A.1(a))

Case 2 is constructed with pattern 1 and 2 for the loading, and pattern 1, 4, 5, and 6 for the unloading. (Figure A.1(b))

Case 3 is constructed with pattern 1,2 and 3 for the loading, and pattern 1, 4, 7, and 8 for the unloading. (Figure A.1(c))

Equations of each pattern are shown as follows.

Pattern 1 (Case 1,2,3)

$$\frac{M}{E_{SMA}bh^2} = \frac{h}{\rho} \left[\frac{E_f}{E_{SMA}} \left\{ \frac{1}{3} \left(\frac{h_f}{h} \right)^3 - \frac{1}{2} \frac{\xi_1}{h} \left(\frac{h_f}{h} \right)^2 \right\} + \frac{1}{3} \left\{ 1 - \left(\frac{h_f}{h} \right)^3 \right\} - \frac{1}{2} \frac{\xi_1}{h} \left\{ 1 - \left(\frac{h_f}{h} \right)^2 \right\} \right]$$

where, ξ_1 is the distance of the neutral axis.

$$\frac{\xi_1}{h} = \frac{\left(\frac{E_f}{E_{SMA}} - 1\right) \left(\frac{h_f}{h}\right)^2 + 1}{2 \left\{ \left(\frac{E_f}{E_{SMA}} - 1\right) \left(\frac{h_f}{h}\right) + 1 \right\}}$$

Pattern 2 (Case 2, 3)

$$\frac{M}{E_{SMA} b h^2} = \frac{h}{\rho} \left[\frac{E_f}{E_{SMA}} \left\{ \frac{1}{3} \left(\frac{h_f}{h}\right)^3 - \frac{1}{2} \frac{\xi_2}{h} \left(\frac{h_f}{h}\right)^2 \right\} + \frac{1}{3} \left\{ \left(\frac{y_1}{h}\right)^3 - \left(\frac{h_f}{h}\right)^3 \right\} - \frac{1}{2} \frac{\xi_2}{h} \left\{ \left(\frac{y_1}{h}\right)^2 - \left(\frac{h_f}{h}\right)^2 \right\} \right] + \frac{1}{2} \frac{\sigma_0}{E_{SMA}} \left\{ 1 - \left(\frac{y_1}{h}\right)^2 \right\}$$

where, ξ_2 is the distance of the neutral axis, and y_1 is the position for $\sigma = \sigma_0$.

$$\frac{\xi_2}{h} = \left\{ \left(\frac{E_f}{E_{SMA}} - 1\right) \frac{h_f}{h} + \frac{\sigma_0 \rho}{E_{SMA} h} \right\} + \sqrt{\frac{E_f}{E_{SMA}} \left(\frac{E_f}{E_{SMA}} - 1\right) \left(\frac{h_f}{h}\right)^2 + 2 \frac{\sigma_0 \rho}{E_{SMA} h} \left\{ 1 + \left(\frac{E_f}{E_{SMA}} - 1\right) \frac{h_f}{h} \right\}}$$

$$\frac{y_1}{h} = \frac{\xi_2}{h} + \frac{\sigma_0 \rho}{E_{SMA} h}$$

Pattern 3 (Case 3)

$$\frac{M}{E_{SMA} b h^2} = \frac{h}{\rho} \frac{E_f}{E_{SMA}} \left\{ \frac{1}{3} \left(\frac{h_f}{h}\right)^3 - \frac{1}{2} \frac{\xi_3}{h} \left(\frac{h_f}{h}\right)^2 \right\} + \frac{1}{2} \frac{\sigma_0}{E_{SMA}} \left\{ 1 - \left(\frac{h_f}{h}\right)^2 \right\}$$

where, ξ_3 is the distance of the neutral axis.

$$\frac{\xi_3}{h} = \frac{\sigma_0 \rho}{E_f h} \left(\frac{h}{h_f} - 1 \right) + \frac{1}{2} \frac{h_f}{h}$$

Pattern 4 (Case 2, 3)

$$\frac{M}{E_{SMA} b h^2} = \frac{h}{\rho} \left[\frac{E_f}{E_{SMA}} \left\{ \frac{1}{3} \left(\frac{h_f}{h}\right)^3 - \frac{1}{2} \frac{\xi_4}{h} \left(\frac{h_f}{h}\right)^2 \right\} + \frac{1}{3} \left\{ \left(\frac{y_2}{h}\right)^3 - \left(\frac{h_f}{h}\right)^3 \right\} - \frac{1}{2} \frac{\xi_4}{h} \left\{ \left(\frac{y_2}{h}\right)^2 - \left(\frac{h_f}{h}\right)^2 \right\} \right] + \frac{1}{2} \frac{\sigma_1}{E_{SMA}} \left\{ 1 - \left(\frac{y_2}{h}\right)^2 \right\}$$

where, ξ_4 is the distance of the neutral axis, and y_2 is the position for $\sigma = \sigma_0$.

$$\frac{\xi_4}{h} = \left\{ \left(\frac{E_f}{E_{SMA}} - 1\right) \frac{h_f}{h} + \frac{\sigma_1 \rho}{E_{SMA} h} \right\} + \sqrt{\frac{E_f}{E_{SMA}} \left(\frac{E_f}{E_{SMA}} - 1\right) \left(\frac{h_f}{h}\right)^2 + 2 \frac{\sigma_1 \rho}{E_{SMA} h} \left\{ 1 + \left(\frac{E_f}{E_{SMA}} - 1\right) \frac{h_f}{h} \right\}}$$

$$\frac{y_2}{h} = \frac{\xi_4}{h} + \frac{\sigma_1 \rho}{E_{SMA} h}$$

Pattern 5 (Case 2)

$$\begin{aligned} \frac{M}{E_{SMA} b h^2} = & \frac{h}{\rho} \left[\frac{1}{3} \left\{ \left(\frac{E_f}{E_{SMA}} - 1 \right) \left(\frac{h_f}{h} \right)^3 + \left(\frac{y_3}{h} \right)^3 \right\} - \frac{1}{2} \frac{\xi_5}{h} \left\{ \left(\frac{E_f}{E_{SMA}} - 1 \right) \left(\frac{h_f}{h} \right)^2 + \left(\frac{y_3}{h} \right)^2 \right\} \right] \\ & - \frac{h}{\rho_1} \left[\frac{1}{3} \left\{ \left(\frac{y_3}{h} \right)^3 - \left(\frac{Y_1}{h} \right)^3 \right\} - \frac{1}{2} \frac{\xi_5}{h} \left\{ \left(\frac{y_3}{h} \right)^2 - \left(\frac{Y_1}{h} \right)^2 \right\} \right] + \frac{1}{2} \frac{\sigma_0}{E_{SMA}} \left\{ \left(\frac{y_3}{h} \right)^2 - \left(\frac{Y_1}{h} \right)^2 \right\} \\ & + \frac{1}{2} \frac{\sigma_1}{E_{SMA}} \left\{ 1 - \left(\frac{y_3}{h} \right)^2 \right\} \end{aligned}$$

where, ξ_5 is the distance of the neutral axis.

$$\frac{\xi_5}{h} = \frac{-B_3 + \sqrt{B_3^2 - A_3 C_3}}{A_3}$$

$$A_3 = 1 - \frac{h \rho}{\rho_1 h}$$

$$B_3 = \left(\frac{E_f}{E_{SMA}} - 1 \right) \frac{h_f}{h} + \left(\frac{h Y_1}{\rho_1 h} - \frac{\sigma_0 - \sigma_1}{E_{SMA}} \right) \frac{\rho}{h}$$

$$C_3 = - \left(\frac{E_f}{E_{SMA}} - 1 \right) \left(\frac{h_f}{h} \right)^2 - \left\{ \left(\frac{h Y_1}{\rho_1 h} - 2 \frac{\sigma_0}{E_{SMA}} \right) \frac{Y_1}{h} + 2 \frac{\sigma_1}{E_{SMA}} - \left(\frac{\sigma_0 - \sigma_1}{E_{SMA}} \right)^2 \frac{\rho_1 \rho}{\rho_1 - \rho} \right\} \frac{\rho}{h}$$

$$\frac{y_3}{h} = \frac{\xi_5}{h} - \frac{\sigma_0 - \sigma_1}{E_{SMA}} \frac{\rho_1}{\rho_1 - \rho} \frac{\rho}{h}$$

$$\frac{Y_1}{h} = \left(\frac{\sigma_f}{E_f} + \frac{\sigma_0}{E_{SMA}} \right) \frac{\rho_1}{h}$$

$$\frac{h}{\rho_1} = \frac{\left(\frac{\sigma_f}{E_f} + \frac{\sigma_0}{E_{SMA}} \right)^2}{- \left\{ \frac{\sigma_f}{E_f} \left(\frac{E_f}{E_{SMA}} - 1 \right) \frac{h_f}{h} - \frac{\sigma_0}{E_{SMA}} \right\} + \sqrt{\left\{ \frac{\sigma_f}{E_f} \left(\frac{E_f}{E_{SMA}} - 1 \right) \frac{h_f}{h} - \frac{\sigma_0}{E_{SMA}} \right\}^2 + \left(\frac{\sigma_f}{E_f} + \frac{\sigma_0}{E_{SMA}} \right)^2 \left(\frac{E_f}{E_{SMA}} - 1 \right) \left(\frac{h_f}{h} \right)^2}}$$

Pattern 6 (Case 2)

$$\begin{aligned} \frac{M}{E_{SMA} b h^2} = & \frac{h}{\rho} \left[\frac{E_f}{E_{SMA}} \left\{ \frac{1}{3} \left(\frac{h_f}{h} \right)^3 - \frac{1}{2} \frac{\xi_6}{h} \left(\frac{h_f}{h} \right)^2 \right\} + \frac{1}{3} \left\{ 1 - \left(\frac{h_f}{h} \right)^3 \right\} - \frac{1}{2} \frac{\xi_6}{h} \left\{ 1 - \left(\frac{h_f}{h} \right)^2 \right\} \right] \\ & - \frac{h}{\rho_1} \left[\frac{1}{3} \left\{ 1 - \left(\frac{Y_1}{h} \right)^3 \right\} - \frac{1}{2} \frac{\xi_6}{h} \left\{ 1 - \left(\frac{Y_1}{h} \right)^2 \right\} \right] + \frac{1}{2} \frac{\sigma_0}{E_{SMA}} \left\{ 1 - \left(\frac{Y_1}{h} \right)^2 \right\} \end{aligned}$$

where, ξ_6 is the distance of the neutral axis.

$$\frac{\xi_6}{h} = \frac{\left(\frac{E_f}{E_{SMA}} - 1\right) \left(\frac{h_f}{h}\right)^2 + 1 - \left\{ \frac{h}{\rho_1} \left(1 + \frac{Y_1}{h}\right) - 2 \frac{\sigma_0}{E_{SMA}} \right\} \left(1 - \frac{Y_1}{h}\right) \frac{\rho}{h}}{2 \left\{ \left(\frac{E_f}{E_{SMA}} - 1\right) \left(\frac{h_f}{h}\right) + 1 - \frac{h}{\rho_1} \left(1 - \frac{Y_1}{h}\right) \frac{\rho}{h} \right\}}$$

Pattern 7 (Case 3)

$$\begin{aligned} \frac{M}{E_{SMA} b h^2} &= \frac{h}{\rho} \left[\frac{1}{3} \left\{ \left(\frac{E_f}{E_{SMA}} - 1\right) \left(\frac{h_f}{h}\right)^3 + \left(\frac{y_4}{h}\right)^3 \right\} - \frac{1}{2} \frac{\xi_7}{h} \left\{ \left(\frac{E_f}{E_{SMA}} - 1\right) \left(\frac{h_f}{h}\right)^2 + \left(\frac{y_4}{h}\right)^2 \right\} \right] \\ &\quad - \frac{h}{\rho_2} \left[\frac{1}{3} \left\{ \left(\frac{y_4}{h}\right)^3 - \left(\frac{h_f}{h}\right)^3 \right\} - \frac{1}{2} \frac{\xi_7}{h} \left\{ \left(\frac{y_4}{h}\right)^2 - \left(\frac{h_f}{h}\right)^2 \right\} \right] + \frac{1}{2} \frac{\sigma_0}{E_{SMA}} \left\{ \left(\frac{y_4}{h}\right)^2 - \left(\frac{h_f}{h}\right)^2 \right\} \\ &\quad + \frac{1}{2} \frac{\sigma_1}{E_{SMA}} \left\{ 1 - \left(\frac{y_4}{h}\right)^2 \right\} \end{aligned}$$

where, ξ_7 is the distance of the neutral axis.

$$\frac{\xi_7}{h} = \frac{-B_4 + \sqrt{B_4^2 - A_4 C_4}}{A_4}$$

$$A_4 = 1 - \frac{h}{\rho_2} \frac{\rho}{h}$$

$$B_4 = \left(\frac{E_f}{E_{SMA}} - 1\right) \frac{h_f}{h} + \left(\frac{h}{\rho_2} \frac{h_f}{h} - \frac{\sigma_0 - \sigma_1}{E_{SMA}}\right) \frac{\rho}{h}$$

$$C_4 = -\left(\frac{E_f}{E_{SMA}} - 1\right) \left(\frac{h_f}{h}\right)^2 - \left\{ \left(\frac{h}{\rho_2} \frac{h_f}{h} - 2 \frac{\sigma_0}{E_{SMA}}\right) \frac{h_f}{h} + 2 \frac{\sigma_1}{E_{SMA}} - \left(\frac{\sigma_0 - \sigma_1}{E_{SMA}}\right)^2 \frac{\rho_2 \rho}{\rho_2 - \rho} \right\} \frac{\rho}{h}$$

$$\frac{y_4}{h} = \frac{\xi_7}{h} - \frac{\sigma_0 - \sigma_1}{E_{SMA}} \frac{\rho_2}{\rho_2 - \rho} \frac{\rho}{h}$$

$$\frac{h}{\rho_2} = 2 \frac{h}{h_f} \left\{ \frac{\sigma_f}{E_f} - \frac{\sigma_0}{E_f} \left(\frac{h}{h_f} - 1\right) \right\}$$

Pattern 8 (Case 3)

$$\begin{aligned} \frac{M}{E_{SMA} b h^2} &= \frac{h}{\rho} \left[\frac{E_f}{E_{SMA}} \left\{ \frac{1}{3} \left(\frac{h_f}{h}\right)^3 - \frac{1}{2} \frac{\xi_8}{h} \left(\frac{h_f}{h}\right)^2 \right\} + \frac{1}{3} \left\{ 1 - \left(\frac{h_f}{h}\right)^3 \right\} - \frac{1}{2} \frac{\xi_8}{h} \left\{ 1 - \left(\frac{h_f}{h}\right)^2 \right\} \right] \\ &\quad - \frac{h}{\rho_2} \left[\frac{1}{3} \left\{ 1 - \left(\frac{h_f}{h}\right)^3 \right\} - \frac{1}{2} \frac{\xi_8}{h} \left\{ 1 - \left(\frac{h_f}{h}\right)^2 \right\} \right] + \frac{1}{2} \frac{\sigma_0}{E_{SMA}} \left\{ 1 - \left(\frac{h_f}{h}\right)^2 \right\} \end{aligned}$$

where, ξ_8 is the distance of the neutral axis.

$$\frac{\xi_{58}}{h} = \frac{\left(\frac{E_f}{E_{SMA}} - 1\right) \left(\frac{h_f}{h}\right)^2 + 1 - \left\{ \frac{h}{\rho_2} \left(1 + \frac{h_f}{h}\right) - 2 \frac{\sigma_0}{E_{SMA}} \right\} \left(1 - \frac{h_f}{h}\right) \frac{\rho}{h}}{2 \left\{ \left(\frac{E_f}{E_{SMA}} - 1\right) \left(\frac{h_f}{h}\right) + 1 - \frac{h}{\rho_2} \left(1 - \frac{h_f}{h}\right) \frac{\rho}{h} \right\}}$$

USEFUL RANGE

The useful range of the curvature of each pattern is shown as follows.

Case 1

Pattern 1 (Loading and Unloading)

$$0 \leq \frac{h}{\rho} \leq \frac{\sigma_f}{E_f} \frac{2 \left\{ 1 + \left(\frac{E_f}{E_{SMA}} - 1\right) \left(\frac{h_f}{h}\right) \right\}}{1 + \left(\frac{E_f}{E_{SMA}} - 1\right) \left(\frac{h_f}{h}\right)^2}$$

Case 2

Pattern 1 (Loading)

$$0 \leq \frac{h}{\rho} \leq \frac{\sigma_0}{E_{SMA}} \frac{2 \left\{ 1 + \left(\frac{E_f}{E_{SMA}} - 1\right) \left(\frac{h_f}{h}\right) \right\}}{1 + \left(\frac{E_f}{E_{SMA}} - 1\right) \left(2 - \frac{h_f}{h}\right) \left(\frac{h_f}{h}\right)}$$

Pattern 2 (Loading)

$$\frac{\sigma_0}{E_{SMA}} \frac{2 \left\{ 1 + \left(\frac{E_f}{E_{SMA}} - 1\right) \left(\frac{h_f}{h}\right) \right\}}{1 + \left(\frac{E_f}{E_{SMA}} - 1\right) \left(2 - \frac{h_f}{h}\right) \left(\frac{h_f}{h}\right)} < \frac{h}{\rho} \leq \frac{h}{\rho_1}$$

Pattern 1 (Unloading)

$$0 \leq \frac{h}{\rho} \leq \frac{\sigma_1}{E_{SMA}} \frac{2 \left\{ 1 + \left(\frac{E_f}{E_{SMA}} - 1\right) \left(\frac{h_f}{h}\right) \right\}}{1 + \left(\frac{E_f}{E_{SMA}} - 1\right) \left(2 - \frac{h_f}{h}\right) \left(\frac{h_f}{h}\right)}$$

Pattern 4 (Unloading)

$$\frac{\sigma_1}{E_{SMA}} \frac{2 \left\{ 1 + \left(\frac{E_f}{E_{SMA}} - 1 \right) \left(\frac{h_f}{h} \right) \right\}}{1 + \left(\frac{E_f}{E_{SMA}} - 1 \right) \left(2 - \frac{h_f}{h} \right) \left(\frac{h_f}{h} \right)} < \frac{h}{\rho} \leq \frac{2 \frac{\sigma_1}{E_{SMA}} \left\{ 1 + \left(\frac{E_f}{E_{SMA}} - 1 \right) \left(\frac{h_f}{h} \right) \right\}}{\left(\frac{Y_1}{h} \right)^2 + \left(\frac{E_f}{E_{SMA}} - 1 \right) \left(2 \frac{Y_1}{h} - \frac{h_f}{h} \right) \left(\frac{h_f}{h} \right)}$$

Pattern 5 (Unloading)

$$\frac{2 \frac{\sigma_1}{E_{SMA}} \left\{ 1 + \left(\frac{E_f}{E_{SMA}} - 1 \right) \left(\frac{h_f}{h} \right) \right\}}{\left(\frac{Y_1}{h} \right)^2 + \left(\frac{E_f}{E_{SMA}} - 1 \right) \left(2 \frac{Y_1}{h} - \frac{h_f}{h} \right) \left(\frac{h_f}{h} \right)} < \frac{h}{\rho} \leq \frac{2A_1}{-B_1 - \sqrt{B_1^2 - 4A_1C_1}}$$

where,

$$A_1 = \left\{ 2 \frac{\sigma_1}{E_{SMA}} + \left(1 - \frac{Y_1}{h} \right) \frac{h}{\rho_1} \right\} \left(1 - \frac{Y_1}{h} \right)$$

$$B_1 = 2 \left\{ \left(\frac{E_f}{E_{SMA}} - 1 \right) \frac{h_f}{h} + 1 \right\} \left(\frac{\sigma_0 - \sigma_1}{E_{SMA}} \frac{\rho_1}{h} - 1 \right) + \left(\frac{E_f}{E_{SMA}} - 1 \right) \left(\frac{h_f}{h} \right)^2 + 1 - \left(1 - \frac{Y_1}{h} \right) \left(1 - \frac{Y_1}{h} + 2 \frac{\sigma_0}{E_{SMA}} \frac{\rho_1}{h} \right)$$

$$C_1 = \frac{\rho_1}{h} \left\{ \left(\frac{E_f}{E_{SMA}} - 1 \right) \left(2 - \frac{h_f}{h} \right) \frac{h_f}{h} + 1 \right\}$$

Pattern 6 (Unloading)

$$\frac{2A_1}{-B_1 - \sqrt{B_1^2 - 4A_1C_1}} < \frac{h}{\rho} \leq \frac{h}{\rho_1}$$

Case 3

Pattern 1 (Loading)

$$0 \leq \frac{h}{\rho} \leq \frac{\sigma_0}{E_{SMA}} \frac{2 \left\{ 1 + \left(\frac{E_f}{E_{SMA}} - 1 \right) \left(\frac{h_f}{h} \right) \right\}}{1 + \left(\frac{E_f}{E_{SMA}} - 1 \right) \left(2 - \frac{h_f}{h} \right) \left(\frac{h_f}{h} \right)}$$

Pattern 2 (Loading)

$$\frac{\sigma_0}{E_{SMA}} \frac{2 \left\{ 1 + \left(\frac{E_f}{E_{SMA}} - 1 \right) \left(\frac{h_f}{h} \right) \right\}}{1 + \left(\frac{E_f}{E_{SMA}} - 1 \right) \left(2 - \frac{h_f}{h} \right) \left(\frac{h_f}{h} \right)} < \frac{h}{\rho} \leq 2 \frac{h}{h_f} \left\{ \frac{\sigma_0}{E_{SMA}} + \frac{\sigma_0}{E_f} \left(\frac{h_f}{h} - 1 \right) \right\}$$

Pattern 3 (Loading)

$$2 \frac{h}{h_f} \left\{ \frac{\sigma_0}{E_{SMA}} + \frac{\sigma_0}{E_f} \left(\frac{h_f}{h} - 1 \right) \right\} < \frac{h}{\rho} \leq \frac{h}{\rho_2}$$

Pattern 1 (Unloading)

$$0 \leq \frac{h}{\rho} \leq \frac{\sigma_1}{E_{SMA}} \frac{2 \left\{ 1 + \left(\frac{E_f}{E_{SMA}} - 1 \right) \left(\frac{h_f}{h} \right) \right\}}{1 + \left(\frac{E_f}{E_{SMA}} - 1 \right) \left(2 - \frac{h_f}{h} \right) \left(\frac{h_f}{h} \right)}$$

Pattern 4 (Unloading)

$$\frac{\sigma_1}{E_{SMA}} \frac{2 \left\{ 1 + \left(\frac{E_f}{E_{SMA}} - 1 \right) \left(\frac{h_f}{h} \right) \right\}}{1 + \left(\frac{E_f}{E_{SMA}} - 1 \right) \left(2 - \frac{h_f}{h} \right) \left(\frac{h_f}{h} \right)} < \frac{h}{\rho} \leq \frac{2 \frac{\sigma_1}{E_{SMA}} \left\{ 1 + \left(\frac{E_f}{E_{SMA}} - 1 \right) \left(\frac{h_f}{h} \right) \right\}}{\left(\frac{Y_1}{h} \right)^2 + \left(\frac{E_f}{E_{SMA}} - 1 \right) \left(2 \frac{Y_1}{h} - \frac{h_f}{h} \right) \left(\frac{h_f}{h} \right)}$$

Pattern 7 (Unloading)

$$\frac{2 \frac{\sigma_1}{E_{SMA}} \left\{ 1 + \left(\frac{E_f}{E_{SMA}} - 1 \right) \left(\frac{h_f}{h} \right) \right\}}{\left(\frac{Y_1}{h} \right)^2 + \left(\frac{E_f}{E_{SMA}} - 1 \right) \left(2 \frac{Y_1}{h} - \frac{h_f}{h} \right) \left(\frac{h_f}{h} \right)} < \frac{h}{\rho} \leq \frac{2A_2}{-B_2 - \sqrt{B_2^2 - 4A_2C_2}}$$

where,

$$A_2 = \left\{ 2 \frac{\sigma_1}{E_{SMA}} + \left(1 - \frac{h_f}{h} \right) \frac{h}{\rho_2} \right\} \left(1 - \frac{h_f}{h} \right)$$

$$B_2 = 2 \left\{ \left(\frac{E_f}{E_{SMA}} - 1 \right) \frac{h_f}{h} + 1 \right\} \left(\frac{\sigma_0 - \sigma_1 \rho_2}{E_{SMA} h} - 1 \right) + \left(\frac{E_f}{E_{SMA}} - 1 \right) \left(\frac{h_f}{h} \right)^2 + 1 - \left(1 - \frac{h_f}{h} \right) \left(1 - \frac{h_f}{h} + 2 \frac{\sigma_0 \rho_2}{E_{SMA} h} \right)$$

$$C_2 = \frac{\rho_2}{h} \left\{ \left(\frac{E_f}{E_{SMA}} - 1 \right) \left(2 - \frac{h_f}{h} \right) \frac{h_f}{h} + 1 \right\}$$

Pattern 8 (Unloading)

$$\frac{2A_2}{-B_2 - \sqrt{B_2^2 - 4A_2C_2}} < \frac{h}{\rho} \leq \frac{h}{\rho_2}$$

Appendix B: List of Publications and U.S. Patents

1. Papers in journals

- [1] Li, J.F., Takagi, K., Ono, M., Pan, W., Watanabe, R., Almajid, A., and Taya, M., "Fabrication and Evaluation of Porous Piezoelectric Ceramics and Porosity-Graded Piezoelectric Actuators", *J. Am. Ceram. Soc.*, 2003, vol. 86, pp.1094-1098.
- [2] Taya, M., Almajid, A., Dunn, M., and Takahashi, H., "Design of Bimorph Piezo Composite Actuators with Functionally Graded Microstructure", *Sensors and Actuators A107.*, 2003, pp.248-260.
- [3] Kusuka, M., and Taya, M., "Design of Ferromagnetic Shape Memory Alloy Composites", *J. Composite Materials*, vol.38, no.12, 2004, pp.1011-1035.

2. Papers in conference proceedings

- [1] Matsunaga, Y., Tagawa, T., Wada, T., and Taya, M., "Design of Ferromagnetic Shape Memory Alloy Composites based on TiNi for robust and fast actuators", proceedings of SPIE on Smart Structure and Materials, San Diego, March 17-21, 2002, vol.4699, pp.172-181.
- [2] Almajid, A., Taya, M., Li, J.F., Takagi, R., and Watanabe, R., "Fabrication and Modeling of Porous Bimorph Piezoelectric Actuators", proceedings of SPIE on smart Structure and Materials, San Diego, March 17-21, 2002, vol.4701, pp.467-476.
- [3] Matsunaga, Y., and Taya, M., "Characterization of TiNi Shape Memory Alloy Composites", proceedings of the 10th US-Japan Conference on Composite Materials, edited by F. K. Chang, DEStech Publications, Lanchester, PA, Sept.16-18, 2002, Keynote paper, pp.40-50.
- [4] Taya, M., Almajid, A., Liang, Y., and Popovic, S., "Modeling of Active Materials", Keynote paper, proceedings of JSME/ASME meeting on Materials and Processing, Waikiki, Hawaii, Oct. 15-17, 2002, vol.1, pp.1-5.
- [5] Wada, T., Taya, M., Chen, H.H., Kusuka, M., "Design of Spring Actuators made of Ferromagnetic Shape Memory Alloys and Composites", *Proc. of SPIE Symposium on Applications*, Ed. E. White, San Diego, CA, March 2-6, 2003, vol.5054, pp.125-134.
- [6] Taya, M., Wada, T., Lee, C.C., Kusuka, M., "Design of Torque Actuators made of Ferromagnetic Shape Memory Alloys and Composites", *Proc. of SPIE Symposium on Applications*, Ed. E. White, San Diego, CA, March 2-6, 2003, vol.5054, pp.156-164.
- [7] Takagi, K., Li, J.F., Watanabe, R., Almajid, A., and Taya, M., "Development of Piezoelectric Ceramic Actuators with Graded Porosity", *Proc. 7th Intl. Symp on Functionally Graded Materials*. Oct 15-18, 2002, Beijing, eds. W. Pan and J.G. Gong, L.M. Zhang, and L.D. Chen, *J. Mater. Forum*, Vol. 423-425, (2003), pp.405-410.
- [8] Li, J.F., Takagi, K., Yokoyama, S., Watanabe, R., Almajid, A., and Taya, M., "Piezo Ceramic/Metal Bending Actuators with Functionally Graded Microstructure", *Proc. 7th Intl. Symp on Functionally Graded Materials*. Oct 15-18, 2002, Beijing, eds. W. Pan and J.G. Gong, L.M. Zhang, and L.D. Chen, *J. Mater. Forum*, Vol. 423-425, (2003), pp.405-410.

- [9] Kuga, Y., Lee, S.W., Almajid, A., Taya, M., Li, J.F., and Watanabe, R., "Experimental and Numerical Studies of Microwave Properties of BaTiO₃-Pt Composites", Proc. of symp.
- [10] Cheng, V., Taya, M., Lee, J.K., Kusuka, M., and Wada, T., "Design of Torque Actuator Based on Ferromagnetic Shape Memory Alloy Composite", Proc. of SPIE on Smart Structures and Materials, 2004, March 14-18, San Diego, vol. 5390, pp. 309-316.
- [11] Gururaja, S., Taya, M., Nakayama, H., Kang, Y.S., Kawasaki, A., and Sutou, Y., "Effective Magnetic Properties of Fe-NiTi (FSMA) Particulate Composite", Proc of SPIE on Smart Structures and Materials, March 6-10, 2005, San Diego.

3. Records of Inventions at UW and U.S. Patents

- [1] U.S. Patent, 10/790, 634, "Design of Ferromagnetic Shape Memory Alloy Composites and Actuators incorporating such Materials", filed 2/27/04 and published on 1/6/05.
- [2] 7290D, "Design of Flying Insect Robots based on Ferromagnetic Shape Memory Alloys and its composites", received 6/9/05
- [3] 7339D, "The Second Design of Flying Insect Robot based on Shape Memory Alloy/Permanent Magnet Composites", received 9/21/05